X-ray computed tomography investigation on the geopolymer matrix formation during the binder jetting additive manufacturing process

J. Adrien, H. Elsayed, F. Gobbin, A. Italiano, E. Maire, P. Colombo

Additive Manufacturing 109 (2025) 104852

Contents lists available at ScienceDirect

Additive Manufacturing

journal homepage: www.elsevier.com/locate/addma

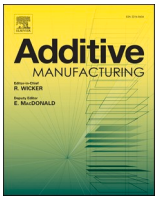

X-ray computed tomography investigation on the geopolymer matrix formation during the binder jetting additive manufacturing process

J. Adrien [a,1], H. Elsayed [b,*,1], F. Gobbin [b], A. Italiano [c], E. Maire [a], P. Colombo [b,d]

[a] Université de Lyon, INSA de Lyon, CNRS, MATEIS UMR5510, Villeurbanne 69621, France
[b] University of Padova, Industrial Engineering Department, Padova, Italy
[c] Desamanera Srl, Rovigo, Italy
[d] Department of Materials Science and Engineering, Pennsylvania State University, University Park, PA 16801, USA

ARTICLE INFO

Keywords:
Geopolymers
Binder Jetting
X-ray Computed Tomography
NMR
Additive Manufacturing

ABSTRACT

This study investigates the geopolymerization mechanism in a binder jetting additive manufacturing system, where a highly alkaline solution is deposited onto a powder bed comprising sand and metakaolin. Two individual alkaline solutions, sodium- and potassium-based, were systematically compared, along with tap water, to interpret processes governing the formation of the geopolymer gel and the subsequent hardening of printed components. Nondestructive volume analysis via X-ray computed tomography was employed to characterize the multiscale structure of the powder bed, while real-time monitoring of alkaline solution–powder bed interactions provided insights into the reaction kinetics as well as material consolidation, from droplet impact to formation of the geopolymer matrix. The results demonstrate successful activation of metakaolin without mechanical mixing, achieved using a large-scale 3D printer with a voxel resolution of $3.0 \times 3.0 \times 3.0$ mm^3 , facilitating the production of large-volume geopolymer components, with an appropriate compressive strength of ~20 MPa, suitable for structural applications. Moreover, Nuclear Magnetic Resonance (NMR) spectroscopy proved the change in the coordination states of aluminium ions, shifting from mixed four-, five-, and six-coordination in metakaolin to predominantly tetrahedral coordination in the final geopolymer. These findings provide critical insights into the microstructural evolution and reaction mechanisms in binder jetting-based geopolymerization.

1. Introduction

In recent years, additive manufacturing techniques have significantly evolved, enabling the creation of complex and customized structures with unprecedented precision and efficiency [1,2]. Among these techniques, Binder Jet Printing (BJP) has received significant attention due to its versatility in processing a wide range of materials, including ceramics, metals, and polymers [3–5].

Concrete and mortars based on Ordinary Portland Cement (OPC) have been explored in additive manufacturing using Binder Jetting Printing (BJP) technology [6]. However, the slow reactivity of OPC during the early stages of hydration presents significant challenges, especially for large-scale powder bed printers like the one used in this study. During the binder jetting process, the binder is ejected from nozzles and reacts with the powder bed. Effective retention of the binder, achieved through either rapid setting or reaction-induced solidification, is essential for maintaining the dimensional accuracy of the printed structure and minimizing lateral diffusion into adjacent regions. In such systems, precise control over rheology and rapid setting is critical to maintaining the structural integrity of the printed parts. In the case of OPC, the limited interaction time between the sprayed liquid and the powder bed often results in incomplete hydration, compromising both dimensional accuracy and mechanical performance. In contrast, magnesia cements have demonstrated potential for additive manufacturing applications due to their faster setting characteristics [7]. For example, Gobbin et al. investigated printed components made from magnesium oxide and potassium phosphate powders. While these systems offer improved setting behavior compared to OPC, they still fall short in terms of long-term strength and durability, compared to geopolymer-based formulations [8].

Geopolymers (GP), inorganic binders derived from alkali activation of alumino-silicates, present an attractive alternative, offering rapid

* Correspondence to: Department of Industrial Engineering, University of Padova, Padova 35131, Italy.
E-mail address: hamada.elsayed@unipd.it (H. Elsayed).
[1] These two authors contributed equally to this work and are designated as co-first authors.

https://doi.org/10.1016/j.addma.2025.104852
Received 12 February 2025; Received in revised form 20 May 2025; Accepted 13 June 2025
Available online 14 June 2025

early strength development [9], high durability [10–12], high compressive strength [13], and are more ecologic since their CO_2 footprint is ten times smaller than that of OPC [14].

The polymerization of alumino-silicates, initiated under alkaline conditions at very high pH, occurs at ambient or low temperatures. The mainly non-crystalline three-dimensionally interconnected structure of these materials is obtained through a multi-step geopolymerization reaction. This involves the dissolution of alumino-silicates in a highly alkaline solution to form free SiO_4 and AlO_4 hydrated species, followed by the diffusion of dissolved Al and Si complexes from the particle surface to the interparticle space, inducing the formation of a gel phase, and finally, the hardening of the gel phase via condensation reactions to form the geopolymer, comprising amorphous to semi-crystalline structures similar to zeolites. The typical chemical formula of a geopolymer is expressed as $Mn[-(SiO_2)zAlO_2]n{\cdot}wH_2O$, where M denotes an alkali cation (Na^+ or K^+), n represents the degree of polymerization, z indicates the Si/Al molar ratio, and w denotes the water content [15].

Despite their many benefits, some aspects still need to be improved, such as brittleness and high drying shrinkage of the hardened geopolymers [16]. This requires a better understanding of their microstructure. Chen et al. [17] have investigated the influence of porosity on the engineering properties of geopolymers in a review. In this study, they categorized the porous network into four length scales, according to their nature:

- Macro pores (greater than 10 μm) mainly due to air bubbles inevitably or intentionally introduced during mixing;
- Meso and micropores, (100 nm - 10 μm) composed of cracks, voids inside or surrounding the unreacted particles, defects and fillers;
- Nanopores, (2 nm - 100 nm) composed of gel interstices in the geopolymer matrix;
- Molecular pores (size below 2 nm) composed of molecular voids in the aluminosilicate network.

The authors highlight the important role played by nanopores and suggest ways of optimizing the properties of geopolymers. The same terminology will be used in the current study.

It has already been successfully demonstrated that geopolymer-based materials can be printed using a variety of techniques [18], including binder jetting [19,20]. In the binder jetting process, the printer deposits raw material powders layer-by-layer, binding them by depositing a liquid on selected areas determined by the 3D digital slice model of the desired object.

Raw material powder properties (such as particle size and distribution, density, flowability, packing, etc.) are of great importance in generating a uniform powder layer, which will form the overall print bed, free of defects that would otherwise end up in the final printed part. It is necessary that the powder possesses good flowability, enabling the printer to deposit a homogeneous layer of particles without forming macro-defects, as happens when a dry fine powder is spread due to the great interparticle forces that tend to bind them together, hindering their flow. Thus, starting powders need to be sufficiently large [21] (generally over 20 μm) and ideally spherical in shape [22].

To address such issues, a granulation process was developed in [23] to obtain a flowable powder, producing a feedstock with suitable flowability comprising granules of sand covered by a high amount of metakaolin (MK, 30 wt%). These relatively spherical particles, with an average size of around 300 μm, consist of a continuous metakaolin thin film around the sand particles, as confirmed morphologically by optical and scanning electron microscopy investigations. Increasing metakaolin in the powder bed throughout the granulation process led to 3D-printed geopolymer parts with a homogeneous microstructure and significant compressive and bending strength (reaching approximately 20 MPa and 8 MPa, respectively, at around 30 vol% total porosity). We tracked the geopolymerization process during binder jetting by determining the phase assemblage changes using X-ray diffraction analysis and by monitoring the formation of the geopolymer using FTIR. However, we believe that more investigations into the alkaline solution–powder bed interactions, setting time, and geopolymer gel formation and hardening are highly needed to improve understanding of the binder jetting additive manufacturing of geopolymer systems.

The work presented here, a continuation of the aforementioned study [23], focuses on monitoring the geopolymer matrix formation, beginning with a precise characterization of the powder bed up to the complete geopolymerization of 3D printed parts via Binder Jetting. For this purpose, X-ray Computed Tomography (XCT) has been widely used. This technique has become an invaluable tool in the study of materials [24] and far beyond, and is of great interest for the characterization of geopolymers because of its unique ability to reveal the three-dimensional microstructure without the need for physical sectioning. Numerous studies present 2D observations using optical or scanning and transmission electron microscopy [25], however, these cannot be obtained during geopolymerisation. In order to better understand these mechanisms, techniques such as XRD and FT-IR can be employed [26,27] but without giving access to direct observation of the microstructure.

In the current study, observations were made on a system consisting of a highly alkaline solution sprayed onto a powder bed combining sand particles with a solid reactive component (metakaolin). Two types of solution were used, one sodium-based, and the other potassium-based alkaline solution. To understand the mechanism of geopolymer gel formation, a comparison with water was also carried out to better understand the phenomena involved as well as the mechanism of geopolymer gel formation, up to the complete hardening of printed parts. In particular, non-destructive volume observations were carried out to obtain a precise description of the starting powder at different scales, from the granule to the powder bed as deposited in the printer. In addition, monitoring was conducted when the various components came into contact, to completely understand the reaction that takes place from the impact of a drop of solution on the powder bed to the formation of the geopolymer matrix. The microstructures obtained during this monitoring were compared with those obtained by manufacturing with a printer.

Furthermore, we demonstrated that the BJP process, employing a large-volume printer with a cubic voxel resolution of $3.0 \times 3.0 \times 3.0\ mm^3$, is capable of successfully activating metakaolin (MK) by directly jetting an alkaline solution on a bed containing reactive alumino-silicate powders, eliminating the need for the vigorous mechanical mixing typically required in conventional geopolymer production. Moreover, to further assess the quality and extent of the geopolymerization reaction, Nuclear Magnetic Resonance (NMR) spectroscopy was conducted.

2. Materials and experimental methods

2.1. Materials

The starting materials were metakaolin, sodium hydroxide, potassium hydroxide, technical grade sodium silicate solution, potassium silicate solution, distilled water and river sand, and the compositions are reported in the Supplementary Material (see Table S1).

Fine metakaolin powder (MK, with D50 of 2 μm, Argical 1200 S, Imerys S.A., France) was used as the aluminosilicate source. The chemical composition of the starting metakaolin was: SiO_2 (55 wt%), Al_2O_3 (39 wt%), Fe_2O_3 (1.8 wt%), TiO_2 (1.5 wt%), $K_2O + Na_2O$ (1 wt%), $CaO + MgO$ (0.6 wt%), with a Loss on Ignition of 1 wt%. The composition of the sodium silicate solution (SS2942, Ingessil S.r.l., Italy) was: SiO_2 (28.35 wt%), Na_2O (9.77 wt%), and H_2O (61.88 wt%). Commercial grade sodium hydroxide (NaOH, Sodium Hydroxide 99 %, HD Chemicals, UK), in the form of flakes, was used. The composition of the potassium silicate solution (MR2,2sperimentale, Ingessil S.r.l., Italy) was: SiO_2 (28.06 wt%), K_2O (19.59 wt%) and H_2O (52.35 wt%). Laboratory-

grade potassium hydroxide (KOH, potassium hydroxide 90 %, Honeywell-Fluka, USA), in the form of a pellet, was used. River sand (RS, with D50 ~0.3 mm and D90 ~0.60 mm, Sabbia Po classica, Bacchi spa, Italy,) was used as unreactive aggregate to reduce the cost of the final printed parts.

2.2. Binder jetting printing process

Given that metakaolin particles typically have a fine size of around 5 μm, we developed a granulation process to produce a feedstock powder bed with adequate flowability, consisting of sand granules coated with metakaolin particles. Therefore, to prepare powder bed mixtures for binder jetting 3D-printing, fine metakaolin powder (MK) was mixed with river sand (RS) in a planetary concrete mixer for 30 min, to produce MK-RS-mixed granulated particles. Afterward, the mixture was sieved to remove particles larger than 1200 μm. Based on our previous findings, the MK:RS weight ratio of 30:70 was selected, and the granules were then labeled as MK30 granules [23].

Two alkaline solutions were prepared to act as the binder jetting liquid for the powder bed. The composition of the two alkaline solutions is reported in the Supplementary Material (see Table S2).

1 - The solution called Na20 was prepared from a sodium silicate solution (SS2942), sodium hydroxide (NaOH) and distilled water, with the following molar ratios: $Na_2O/SiO_2 = 0.8$; $H_2O/Na_2O = 14$ (i.e. 19 wt % SiO_2, 16 wt% Na_2O and 65 wt% H2O);

2 - The solution called K16 was prepared from a potassium silicate solution (MR2,2 sperimentale), potassium hydroxide (KOH) and distilled water, with the following molar ratios $K_2O/SiO_2 = 0.8$; $H_2O/K_2O = 12$ (i.e. 20 wt% SiO_2, 25 wt% K_2O and 55 wt% H_2O).

A 3D large-volume printer based on the binder jetting technology (Desamanera1 60.60 - PaSta, Desamanera s.r.l., Rovigo, Italy), with a printing envelope about 60 × 60 × 60 cm and a cubic voxel resolution of 3.0 × 3.0 × 3.0 mm, was used. The printer possesses a printing head containing 192 nozzles with a diameter of 1 mm. The printer uses a recoating system for generating the powder bed, which operates by depositing a specific volume of the required layer (50 vol%, i.e., half layer with a thickness of 1.5 mm) when moving forward. During this movement, the liquid is also selectively jetted in designated printing areas of the deposited layer. After this, the printer moves backward, depositing the rest of the powder layer through the recoating system, to generate at the end a layer with a thickness of 3 mm. The process is then repeated for the next layers, layer-by-layer, until achieving the printed part. The binder jetting process was performed with a nozzle opening time of 50 ms and 30 ms (for Na20 and K16, respectively) and a printing speed of 20 mm/s, at room temperature with approximately 50 % humidity. Before starting a printing session, we checked the amount of liquid ejected under the target parameters to ensure consistency across the various sample productions and then verified that the solution viscosity was close to the initially measured values: 24.6 cP for the Na20 solution and 69.6 cP for the K16 solution, respectively. After printing, the parts were left to cure in the printing bed overnight. They were then removed from the bed, exhibiting sufficient strength to be handled without issues, and were subsequently further aged and cured for either 7 or 28 days at ambient temperature and humidity.

2.3. X-ray Computed Tomography Characterization

Two different tomographs were employed to investigate the binder jetting process of the geopolymers and understand the gel formation as well as the geopolymerization reaction time.

Firstly, a vtomex device (Baker Hughes Digital Solutions GmbH, Wunstorf, Germany), equipped with a 160 kV nano-focus tube, a tungsten transmitting target, and a 1920 × 1536 pixels Varian detector (pixel size 127 μm), was used for medium-resolution characterizations. The experimental protocol was as follows:

- The metakaolin granules were inserted in a polymer cylinder with an internal diameter of 3 mm and then scanned with a voxel size of 5 μm and the following parameters: voltage of 80 kV, current of 280 μA, exposure time of 333 ms, and 3000 projections collected over 360° with continuous rotation to limit particle movement. The size of the analyzed volume was 3.35 × 3.35 × 2.6 mm. The XCT device used is illustrated in Fig. 1a.
- The powder bed was also scanned using continuous rotation and 4000 projections but with a higher voltage, 140 kV, and a 0.3 mm thick copper filter due to the higher attenuation of these samples, consisting of a polymer container with a 48.5 mm internal diameter filled with powder. The current was 80 μA, and the exposure time was 500 ms. A voxel size of 35 μm was chosen to allow for the characterization of a sufficiently large thickness to highlight any heterogeneity linked to the deposition. The size of the volumes analyzed was 35 × 35 × 38 mm.
- For reaction monitoring, a volume of 0.23 cm of MK30 granules was deposited in a polymer straw with an internal diameter of 5.5 mm. The first acquisition was performed to characterize the powder bed. Then, 5 drops of solution were introduced through the top of the tube using a pipette. This represents a weight of 0.21 g, and it respects the proportions used to print the parts (0.9 g of solution for 1 cm of powder). Acquisition parameters were adapted to reduce the acquisition time. The exposure time was 200 ms, and the number of projections was 900, resulting in a scan time of 3 min. The number of projections was increased to 3000 for the initial and final states to obtain better image quality in these stable states.
- The printed parts were scanned with a voxel size of 5 μm (analyzed volume of 3.35 ×3.35 x 3.4 mm), for a cubic sample of approximately 8 mm on each side, with the following parameters: voltage 80 kV, current 280 μA, exposure time 333 ms, and 1500 projections with an average of 3 images at each angle. The 25 mm square cubic samples were scanned with a voxel size of 15 μm, with the following parameters: voltage 100 kV with a 0.1 mm thick copper filter, intensity 180 μA, exposure time 500 ms, and 1500 projections with an average of 3 images at each angle. The scan time for each of these acquisitions was between 33 and 50 min.

The second tomograph used, designed by the company RX Solutions, was dedicated to high-resolution characterizations and fast radiography monitoring. This tomograph is equipped with a LaB_6 emission tip for the X-ray source, with an actual spot size of 0.25 μm. The resolution is then not modified by geometric blur. The Hammamatsu X-Ray source was operated at a voltage of 100 kV with a current of 150 μA. The detector was a Varian 2520dx with 1920 × 1536 pixels and a pixel size of 127 μm. Acquisitions with a voxel size of 0.3 μm were carried out on granules and samples of printed parts. The volumes analyzed were respectively 0.48 × 0.48 × 0.39 mm and 0.3 × 0.3 × 0.3 mm.

These high-resolution analyses were also carried out on a mixture of granules and Na_2O solution to follow the evolution of the geopolymer gel-formation kinetics as well as the microstructure during geopolymerization. As these acquisitions, carried out at this scale, are considerably longer and require much more sample stability, a special procedure was adopted. A drop of Na20 solution was deposited on a bed of MK30 powder. After approximately 2 min, part of the mixture was introduced into a polymer tube with an internal diameter of 1 mm. Using such a small diameter tube is necessary to place the sample close enough to the X-ray source to achieve the required geometric magnification (see Fig. 1b). Each scan consisted of 2500 projections with an exposure time of 1.66 s and an average of 3 radiographs for each projection. The total time for a scan was 3 h and 30 min. After one day, an initial acquisition was carried out, with special care taken to clearly locate the area to be analyzed. This same area was scanned regularly until more than 100 days after liquid deposition. The sample remained at room temperature between 23 and 25°C during the entire monitoring period. The different volumes obtained were then registered with Fiji,

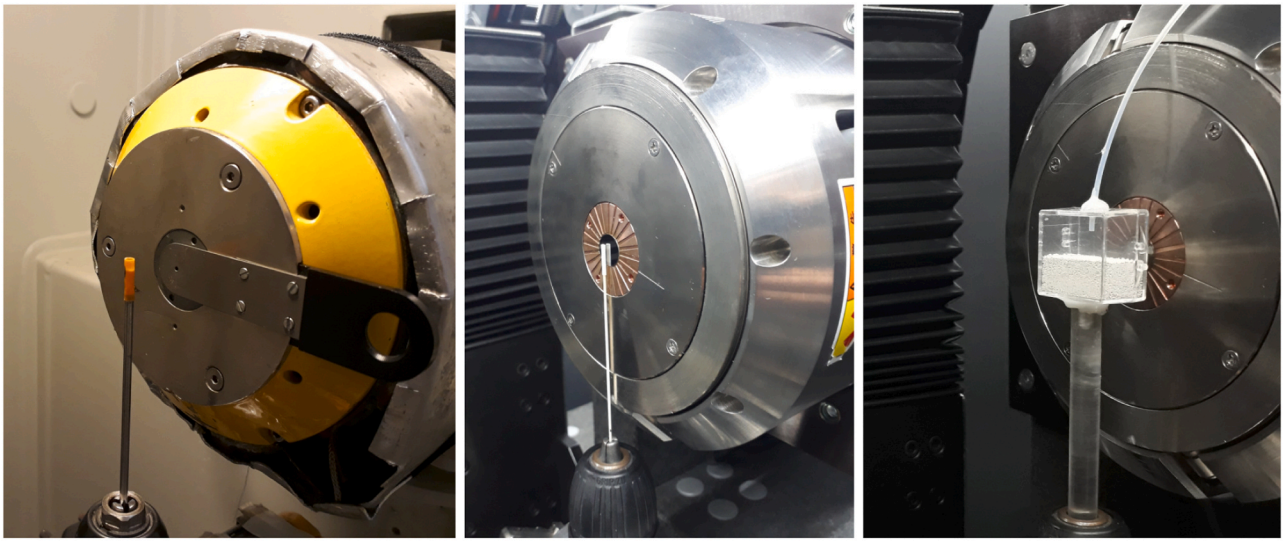

Fig. 1. XCT set up used for: (a) medium-resolution granule characterization and reaction monitoring; (b) high-resolution analysis and (c) X-ray monitoring of interaction between solution drops and powder bed.

first manually and then automatically with the Fijiyama plugin [28]. This procedure enabled us to track the same volume of 0.3 × 0.3 × 0.3 mm.

This system also enabled imaging the interaction between the solution drops and the powder bed to be monitored using fast radiographs, with the drawback being the generation of only a single 2D projection. To this end, 30 images per second were collected with a pixel size of 10 μm and a voltage of 100 kV.A simple device was developed; the powder bed (height ~15 mm) was placed in a box with a section of 6.5 × 30 mm and a height of 30 mm (see Fig. 1c). The alkaline solution (or water for comparison) was injected through a tube, with an inner diameter of 1 mm, that exited outside the self-protected cabin of the tomograph. The quantity of liquid (around 15 mm) is comparable to that deposited during part manufacturing in the actual 3D printer. The distance between the extremity of the tube used to eject the drop and the powder bed (around 10 mm) is slightly greater than the one used in the printer. Its diameter, though, is identical to the nozzle diameter. A slight pressure was applied to the tube to eject the drop of solution, and the setting process was recorded using radiography. Tomographic scans were also taken after the solution was deposited to visualize the zone of interaction with the powder bed. For each scan, 4000 projections were collected during continuous rotation with an exposure time of 150 ms. The total time for a scan was 10 min. The voxel size was 10 μm and the size of the analyzed zone 9 × 9×8.5 mm. The cone-beam XCT data collected with both tomographs were reconstructed by a filtered back-projection Feldkamp algorithm.

2.4. Image analysis

The reconstructed data were processed and visualized with the public domain ImageJ/Fiji shareware [29,30] and Paraview [31] for the 3D rendering. The first step was to present qualitative results using 2D reconstructed slices representing a map of the attenuation in the material. Quantifications were also carried out on volumes. The most straightforward involved thresholding using the grayscale histogram to select the desired element, for example, sand particles. Once this had been done, it was possible to obtain the volume fraction of the element. Density profiles calculated for each slice as a function of its position were also generated to evaluate the homogeneity of the powder bed.

From the binarized volume after thresholding, if the objects are not connected to each other, their properties can be obtained by labeling each cluster of voxels (hereafter names “object”) and then calculating the volume V and outer surface S of each object. The equivalent diameter is calculated ($\underline{D}_{eq}=(6\ V/\pi)^{1/3}$) assuming that the objects are spherical. From this data, a sphericity parameter ($s = 6\ V(\pi/S^3)^{1/2}$) can also be determined [32], values close to 1 corresponding to a perfect sphere and those close to 0 to a very elongated object. This method was applied to sand particles and porosity observed in the printed samples. For the granules, which are in contact with each other, a preliminary watershed step was applied before labeling in order to separate them.

The “local thickness” plugin [33] was used to calculate the thickness of the metakaolin surrounding the sand particles and the size of the voids between the granules. The local thickness is defined as the diameter of the largest sphere that fits inside the object. It can therefore be considered as the smallest lateral dimension of the object.

2.5. NMR analysis

Nuclear magnetic resonance (NMR) spectroscopy analysis was carried out to better evaluate the quality and degree of the geopolymerization reaction, since the aluminum ions spectrum changes from a mixed status of four-, five- and six-coordination typical of metakaolin to the four-coordination tetrahedral status of the final geopolymeric network. The pure metakaolin, Na- and K-activated matrix were analyzed with solid-state nuclear magnetic resonance spectroscopy (Bruker 400Avance WB equipped with double channel 4 mm CPMAS probe, Bruker Spa, Rheinstetten) at 27Al frequency of 104.46 MHz with single π/12 pulse sequence at room temperature at 11 kHz of spinning speed with 1k scans and 3 s recycle delay [34]. All the results of profile fitting, obtained with the Bruker Topspin 3.6 SW, are considered acceptable with a confidence level > 95 %.

2.6. Physical and mechanical properties of the printed parts

The bulk density of the printed pieces was obtained as the ratio between the weight, obtained with an analytical balance with an accuracy of the third digit on a gram, and the volume, measured using a digital caliper. The apparent and true density were measured, on whole samples and their ground powder, using a helium pycnometer (Ultrapyc 3000, Anton Paar, USA). The open and total porosity of the printed parts were then calculated from the ratio between their bulk, apparent, and true density values.

The mechanical properties were evaluated by testing at least 10 samples for each type, using a universal testing machine (Quasar 25, Galdabini spa, Italy) operating with a controlled head speed of 0.5 mm/min. For the flexural strength tests (3-points), printed bars with a dimension of around 30 × 30 × 135 cm and a span of 8 cm were used, while for compressive tests, cubes of 30 × 30 × 30 cm cut from larger samples were used.

3. Results and discussion

3.1. Granules and dry powder bed characterizations

3.1.1. MK30 Granules

High-resolution and medium-resolution characterizations were conducted to provide a qualitative and quantitative description of the MK30 granules before printing. The reconstructed slices obtained from a medium-resolution acquisition, Fig. 2a, allow the visualization of several granules. The sand particles appear bright due to their significant X-ray attenuation (higher grey levels). Some sand particles contain regions with very absorbent phases but this will not be studied in this paper. They are all covered by a layer of metakaolin with lower grey levels. The darkest areas observed between the granules correspond to voids. Not all granules are identical; for example, in the case of the granule labeled 1, a sand particle of a few hundred microns in size is visible in its center. Agglomerates of sand particles are observed inside some other granules (labeled 2), while in other cases, there are no sand particles (or only dust) in the metakaolin, as seen in the granule labeled 3. The MK layer appears to be continuous all around the sand particles, although its thickness is not uniform.

Observations at higher resolution (voxel size of 0.3 μm) reveal strong cohesion between the sand particles and the metakaolin, Fig. 2b. The interface between these two components does not show any defects such as porosities or cracks. Despite the high resolution, it is difficult to clearly dissociate the Metakaolin particles from each other.

The volume fractions of the different components of the granules were determined based on the images obtained at medium resolution in conditions close to what is observed in the powder bed before printing. Thresholding was performed on the grey-level histograms to estimate the volume fraction of sand and Metakaolin as well as the intergranule voids. The different values are reported in Table 1.

The granulation step was carried out in a way to obtain a mixture consisting of 30 wt% of fine metakaolin particles and 70 wt% of river sand. This should theoretically lead to a mixture of approximately 35 vol % metakaolin and 65 vol% sand. The values obtained from the tomography images indicate a higher proportion of metakaolin than sand (closer to a 42/58 ratio). This is certainly due to the fact that the void-metakaolin layer is not fully dense. However, the porosities that may be present between the fine metakaolin particles are not visible at the scale the observations were made. From the theoretical data, the "intra" metakaolin porosity can be deduced based on the volumic ratio MK/RS = (35/65) = 0.538. The density of the metakaolin layer can thus be estimated at 0.387 as well as the internal porosity of the metakaolin (see Table 2). The large volume of residual voids is typical of a powder bed generated by BJP 3D printers [35].

Table 1
The volume fraction of sand - metakaolin - intergranules voids estimated from grey level thresholding of images obtained at a voxel size of 5 μm.

Powder bed components	Volume fraction (%)
Sand	19.7
Metakaolin	27.4
Intergranules Voids	52.9

Fig. 3 reports the histograms depicting the size distribution of the sand particles within the granules and the size distribution of the granules themselves. Equivalent diameters were computed based on the volumes of each object, excluding those in contact with the edges of the analyzed volume. For the granules, a watershed tool was applied in order to separate them. However, this technique faced limitations when applied to sand due to the elongated shape of some particles, leading to fragmentation. Consequently, when multiple particles of sand are present in the same granule, they touch each other, and the measurement reported here corresponds to the size of the group of sand clustered particles.

The size distribution of sand shows a population of small particles with an equivalent diameter of less than 50 μm and another with a larger

Table 2
Estimation of the volume fraction of intra Metakaolin porosity based on the weight fractions of metakaolin and sand in the mixture.

Powder bed components	Volume fraction (%)
Sand	19.7
Metakaolin	10.6
Intrametakaolin porosity	16.8
Intergranule Voids	52.9

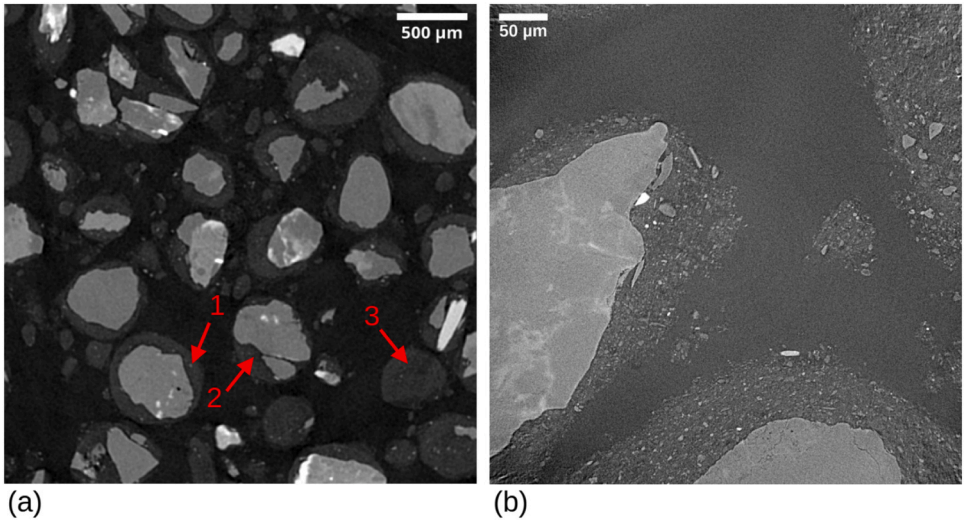

Fig. 2. Reconstructed slices of the MK30 granules (Sand 70 wt% + metakaolin MK 30 wt%) at (a) medium resolution (voxel size 5 μm); and (b) high resolution (voxel size 0.3 μm).

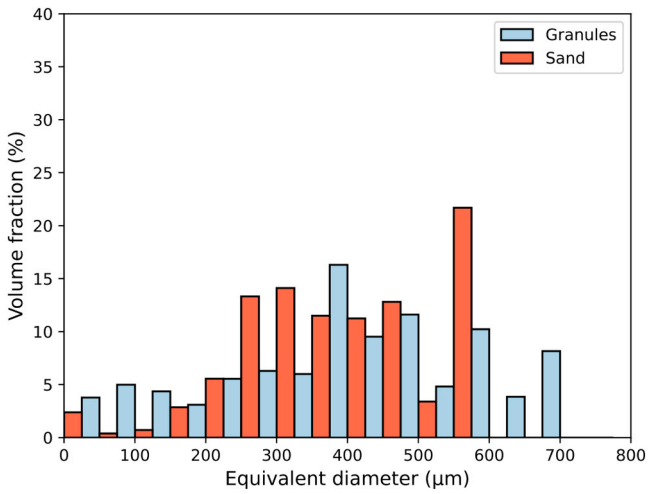

Fig. 3. Histogram representing the equivalent diameter of sand particles (a) and MK30 granules (b).

diameter centered around a value of approximately 350 µm. Objects larger than 500 µm correspond to agglomerates. The size distribution of the granules (comprising both sand and metakaolin) exhibits a first peak of around 150 µm. This one corresponds mainly to the granules with low-size sand particles and to granules in which there is no sand inside. A second peak is centered around 500 µm, it concerns the granules with one or more sand particles inside.

The cumulative particle size distribution of sand particles and MK30 granules was determined. Granulated powders followed a similar size distribution trend as sand particles and were slightly bigger in size, as expected (supplementary material, Figure S1).

The morphology of the granules enclosing a sand particle with a diameter greater than 50 µm was characterized. This value was chosen to exclude the small particles, visible in Fig. 2, which can be considered comprised of sand dust. Consequently, for each granule/sand particle pair, a comparison can be made between their sphericity and equivalent diameter. When several sand particles were included in the same granule, the properties of the agglomerate were considered.

The sphericity values for each individual sand particle (depicted in blue) or sand agglomerate (displayed in red) are plotted against the sphericity of the granule enclosing them in Fig. 4a. 3D renderings are associated with this figure in order to illustrate some cases: a sand agglomerate inside a granule (top left) and a sand particle of low sphericity (0.65) forming a higher sphericity object (0.75) thanks to the metakaolin layer (bottom right).

The graph, in Fig. 4b, presents the size of the sand particles (or agglomerate) as a function of the size of the resulting granules, highlighting the increase caused by the metakaolin layer. The morphological characteristics (sphericity, equivalent diameter) of the sand particles and the resulting granules are shown in Table 3. The mean sphericity and mean equivalent diameter values are separately reported for single and clustered sand particles.

These results offer insights into the impact of the granulation process and the beneficial effect on powder flowability with possibly defect-free powder bed formation. It leads to particles with a more regular shape, without edges or large flat surfaces. Both sphericity and average size demonstrate an increase compared to sand particles (values obtained after the granulation process are above the x = y line, Fig. 4). The amount of small objects, less than 50 µm, is limited. All surfaces are covered with metakaolin, and no cavities entrapped between the sand particles are observed.

The metakaolin and the intergranule void thickness were calculated using the aforementioned granulometry technique (Fig. 5). The metakaolin layer is generally rather thin, less than 100 µm. The thicker zones are the result of the presence of metakaolin granules without sand inside. The size distribution of the intergranule voids in the powder bed is centered on a value of about 150–200 µm, with the maximum size not exceeding 550 µm.

3.1.2. Dry powder bed

The acquisition was also carried out on a dry powder bed collected from the printer after powder deposition of the previously studied granules by the recoating system and without jetting of the alkaline solution, see Fig. 6a. For comparison, the powder bed was also manually poured into a vessel and scanned using the same conditions, Fig. 6c. The graph, in Fig. 6b, shows the profiles of the sand and porosity volume fractions for dry powder beds taken from the printer and poured randomly. The voxel size used is not sufficient to accurately determine the absolute value of the porosity volume fraction, but it nevertheless reveals possible relative variations. Porosity is much smaller in the case of the recoated powder bed compared to the randomly poured powder. No correlation between the 3 mm thick layers deposited by the recoating

Table 3
Morphological characteristics (mean sphericity and mean equivalent diameter) of granules composed of single or clustered sand particles.

	Mean Sphericity	Mean Equivalent diameter (µm)
Sand single particles	0.7	325
Granules with sand single particles	0.73	416
Sand cluster	0.54	384
Granules with sand cluster	0.68	476

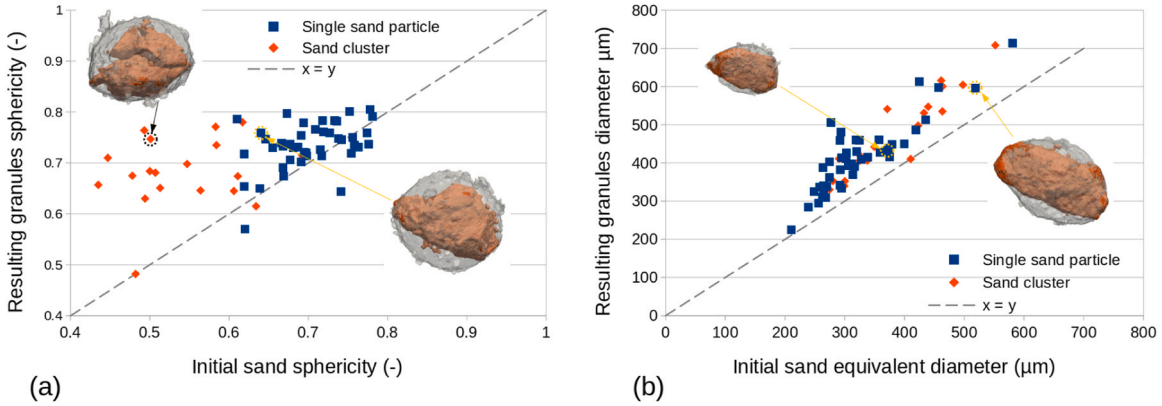

Fig. 4. Graph representing the evolution of the morphology of each sand particle after granulation (a) sphericity (b) equivalent diameter. The x = y lines have been drawn as dotted lines to highlight the effect of the granulation process.

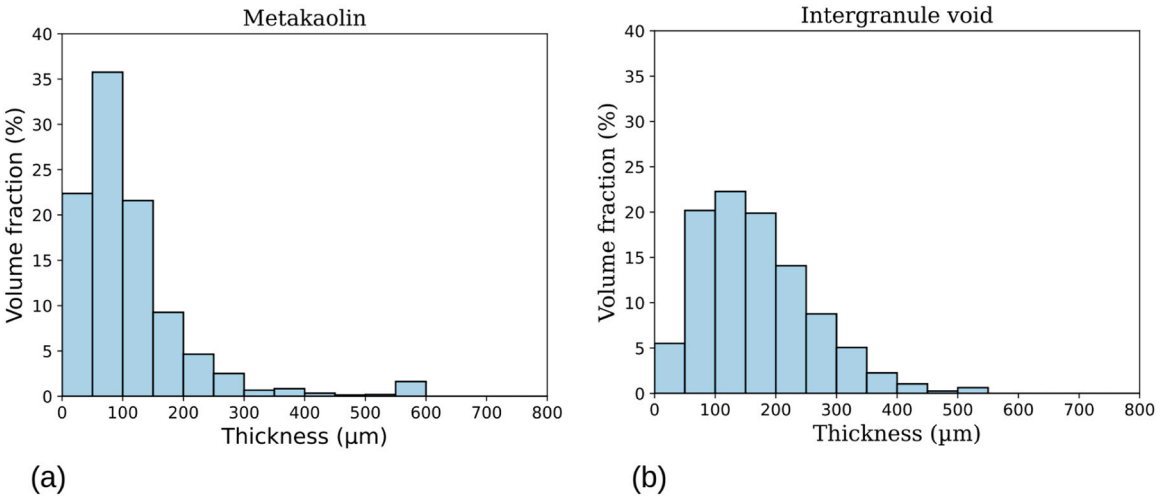

Fig. 5. Histogram representing the metakaolin layer thickness (a); and the intergranule void thickness (b).

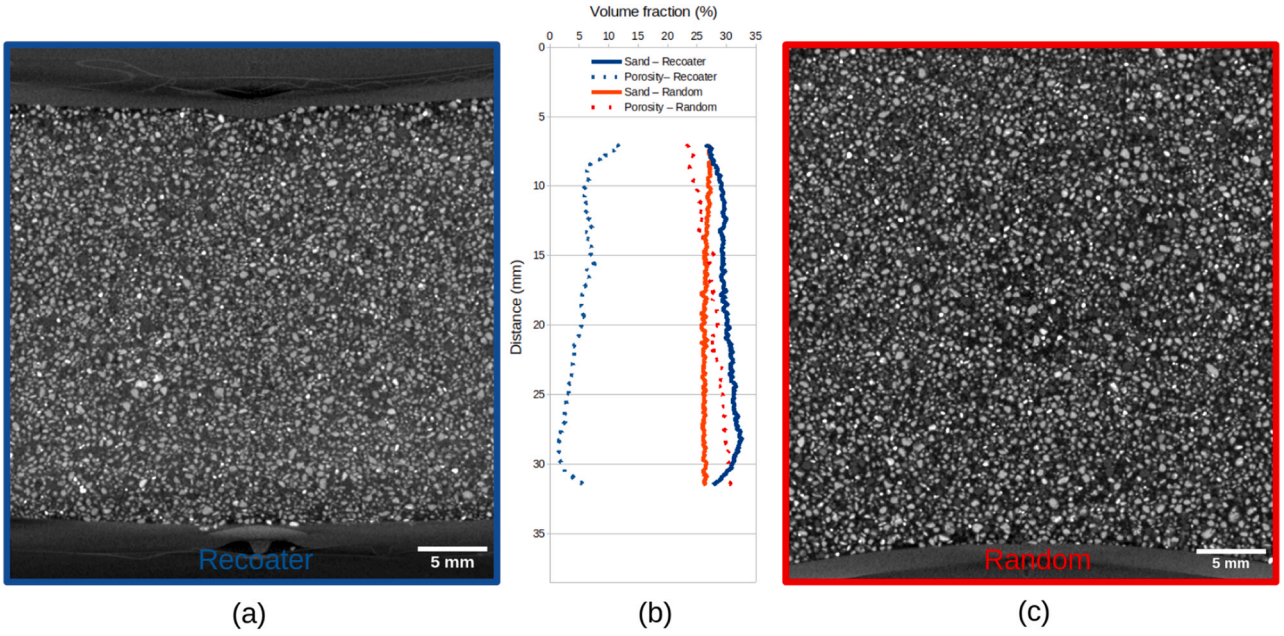

Fig. 6. Reconstructed slices of the dry powder bed along the powder deposition axis: (a) Dry powder bed deposited by the recoater extracted from the printer; (b) Evolution of the volume fraction of sand and porosity; (c) Dry powder bed manually and randomly poured inside a simple parallel epipedic box.

system and the variations in the volume fraction of porosity was observed, as previously revealed by Gobbin et al. [7] using the same procedure for a powder bed composed of river sand mixed with reactive magnesium oxide and potassium phosphate powders (no granulation step, fine powder was free). This further confirms the very positive effect that granulation has on the homogeneity achievable for the produced powder beds.

A small fluctuation of sand volume fraction is observed during recoating, with the value increasing from the surface to the bottom of the powder bed. Regarding the porosity, the volume fraction decreases from the surface to the bottom. The variation in the manually poured powder bed is much smaller and the sample is very homogeneous, although containing a higher fraction of pores. The opposite trend is observed compared to recoater deposition. The volume fraction of sand is slightly higher at the surface and the volume fraction of porosity increases from the surface downwards. It should be noted that with the voxel size of 35 µm, it is only possible to threshold the largest porosities; therefore, their volume fraction is underestimated in both samples.

The main conclusion to be drawn from this comparison is that deposition using the recoating system produces a compact powder bed, rather homogeneous along its height with no strong effect linked to successive layers. The variations observed between the top and bottom of the analyzed volume may indeed be linked to the unperfect powder bed sampling procedure.

3.2. *Interactions between liquid drops and granules*

X-ray radiograph monitoring was conducted to observe the dynamic mechanisms involved during the interaction between a drop of the alkaline solution and the powder bed. The results presented here pertain to the interaction between a single drop and the powder bed. The simplicity of the system used and the space constraints involved do not allow accurate reproduction of the printing device, making quantification of the monitored phenomena difficult. We shall therefore limit our observations to a semi-quantitative comparison of the different alkaline solution binders, i.e., Na20 and K16, that led to geopolymer formation.

Tests were also carried out with pure and neutral water, for comparison, as a liquid binder that does not react with metakaolin powder.

3.2.1. Sodium alkaline solution (Na20)

Fig. 7 displays X-ray radiographs collected up to 10 s after the impact between the drop of Na20 solution and the MK30 powder bed. The observed powder bed height is about 6.5 mm. Time 0 is the time when the drop impacts the powder bed. A single drop is deposited during these tests. Upon impact, a deformation of the drop is first observed, with a slight spreading. The powder bed is also slightly compacted during the impact. In a second phase, probably drawn by capillary forces, the drop gradually penetrates the powder bed. After approx. 2–3 s, the drop has fully migrated below the surface of the powder bed, which reflects the high penetration speed of the alkaline solution binder, facilitating the binder jetting process. This is due to the low viscosity of the alkaline solution and its good wetting of the powder granules' surface.

To better visualize the drop progression within the powder bed, we calculated the difference between the initial radiograph, before impact, and the radiographs after impact, for different times, Fig. 8. These images highlight the compaction of the powder bed upon impact, with changes visible well below the location of the drop on the surface. They also reveal the progression of the interaction zone between the solution and the powder bed, even once the drop is completely below the surface, as it can be seen by comparing the images obtained for times of 3 s and 10 s.

3.2.2. Potassium alkaline solution (K16)

Similar mechanisms were observed for the K16 potassium solution, with deformation of the drop upon contact and compaction of the powder bed followed by gradual migration within the powder bed. The same order of magnitude of time, approximately 2 s, is observed for complete penetration inside the powder bed (supplementary materials, Figures S4 and S5).

3.2.3. Tap Water

The penetration of the drop of water into the powder bed was measured to be much faster, taking around 0.2 s, (see supplementary material, Figure S6 for a radiography series comparable to Fig. 7 above). Due to the short duration of the phenomenon, the evolution of the shape of the droplet during impact was difficult to observe. Regarding the powder bed, no particle movement was detected upon impact in the images, showing the differences between the two liquid media (supplementary material, Figure S7).

The graph, in Fig. 9, depicts the progression of the affected zone over time. These results were obtained by calculating the ratio between the position of the affected zone at time (t) and its final position after approximately 45 s (from this moment on, the solution no longer progresses within the powder bed). Two experiments were conducted for each type of deposited drop, and the results represent the average of these two experiments.

Whatever the nature of the solution, as soon as the drop comes into contact with the powder bed, a significant proportion of the progression of the affected zone is achieved (already around 50 %). Then, these results reveal specific behaviors for the different types of liquid. The interaction zone between the Na20 solution and the powder bed progressed in three stages. During the first stage, progress was relatively

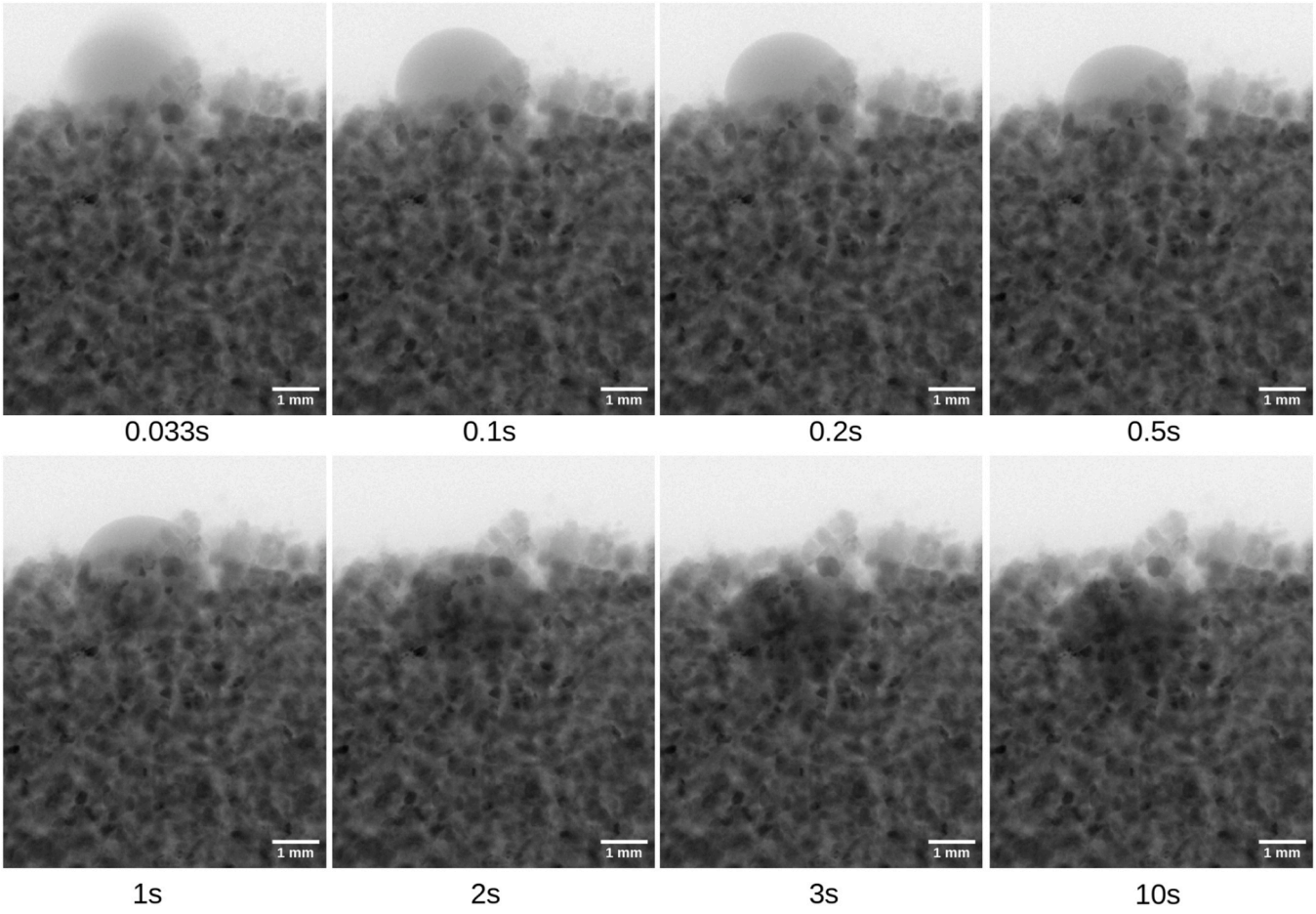

Fig. 7. X-ray radiography sequence during deposition of a drop of Na20 solution on the MK30 powder bed for times between 0.033 s after contact and 10 s, see (supplementary material, Fig. S2).

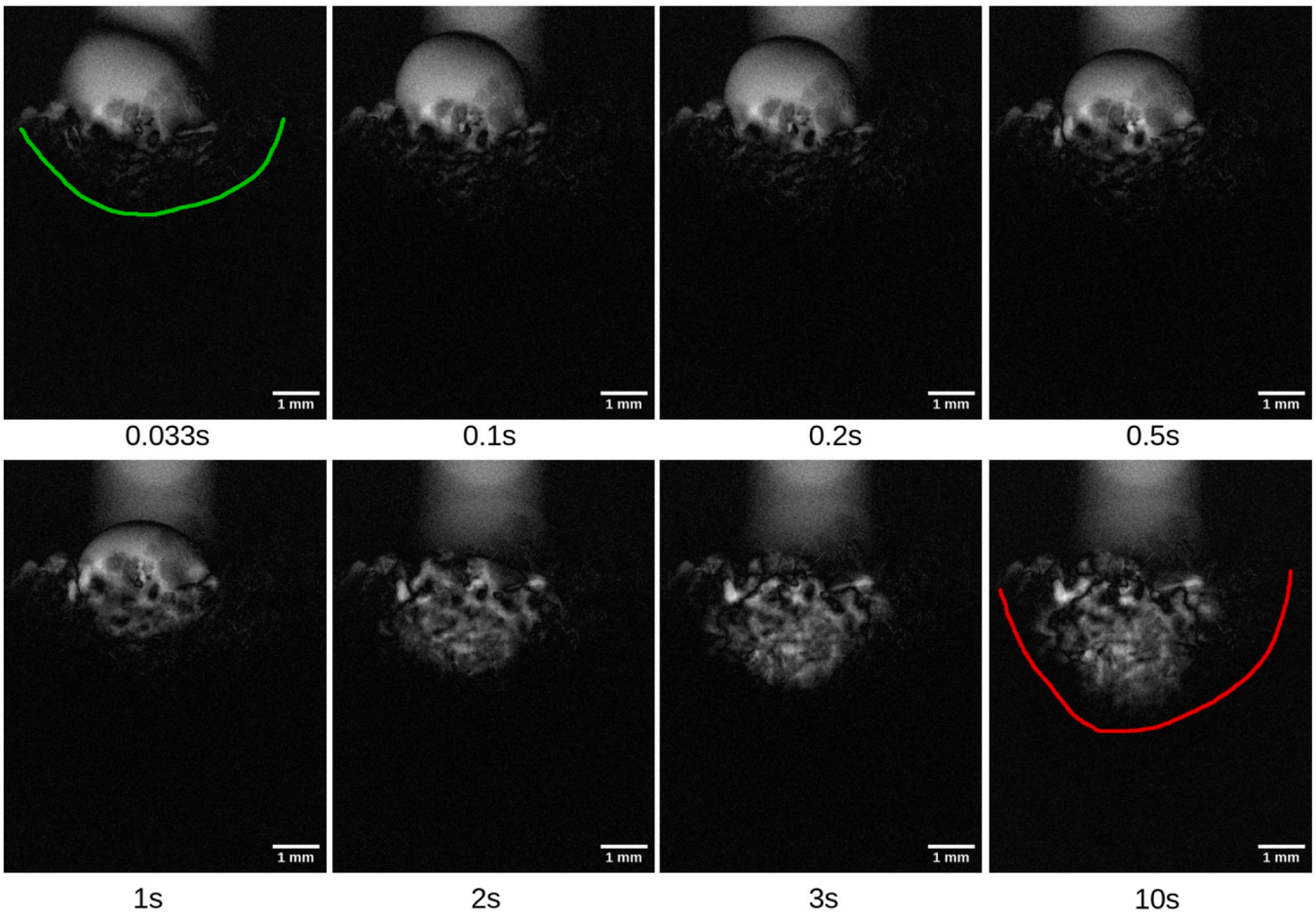

Fig. 8. Difference between a radiograph before the impact of the drop of Na20 solution with the MK30 powder bed and after the impact for different times. The position of the affected zone at time (t) and its extreme position, observed after about 45 s, are shown in green and red respectively, for illustration purposes, see (supplementary material, Fig. S3).

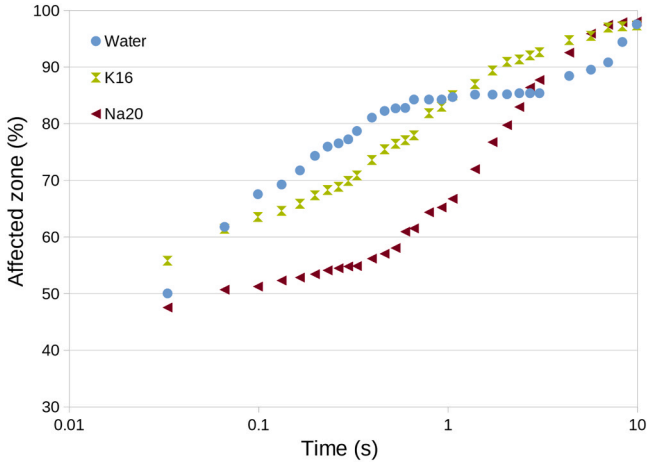

Fig. 9. Progression of the zone affected by the interaction between the drops and the powder bed as a function of time.

slow. An acceleration was noted after a time slightly shorter than that observed for complete penetration of the drop into the powder bed. Finally, after 5 s, a slowdown was observed. The progression in the case of the K16 solution is more regular, with less pronounced stages. Progress is nevertheless faster with this solution than with Na20 on shorter timescales. The higher viscosity of Na20, compared to K16 (24.6 cP vs 69.6 cP), could lead to a lower penetration rate at the initial stage.

The behavior observed in the case of pure water is quite different. First, monitoring reveals a very rapid progression of the affected zone. Then, after approximately 0.5 s, no further evolution was detected. Finally, after 3 s, a new expansion of the affected zone was observed. The faster penetration of water is due to wettability and viscosity differences, as well as the lack of any chemical reaction that instead, occurs between the alkaline solutions and the reactive metakaolin powders.

Tomography scans were acquired after the radio monitoring of the binder solution deposition. XCT characterization performed after the impact between the drop of solution and the powder bed revealed the presence of an agglomerate, Fig. 10. This more compact zone (area surrounded in blue) has a hemispherical shape and contains porosities. This agglomerate certainly corresponds to the volume bonded immediately after the impact of the solution on the powder bed. The densification of this zone resulted from MK's dissolution after drop liquid deposition, leading to geopolymer gel formation, and thereby geopolymer formation matrix. It is also probable that the metakaolin powders partly detach from the granule when in contact with the alkaline solution, leading to an easier filling of the intergranule voids. The upper surface of the agglomerate is relatively flat and does not exhibit a marked dimple, as previously evidenced with reactive magnesium oxide- potassium phosphate and sand powders [7]. Those powders were certainly more "volatile" upon impact, than metakaolin granules, and this is another advantage provided by the granulation approach.

The agglomerates are surrounded by isolated granules (in the area

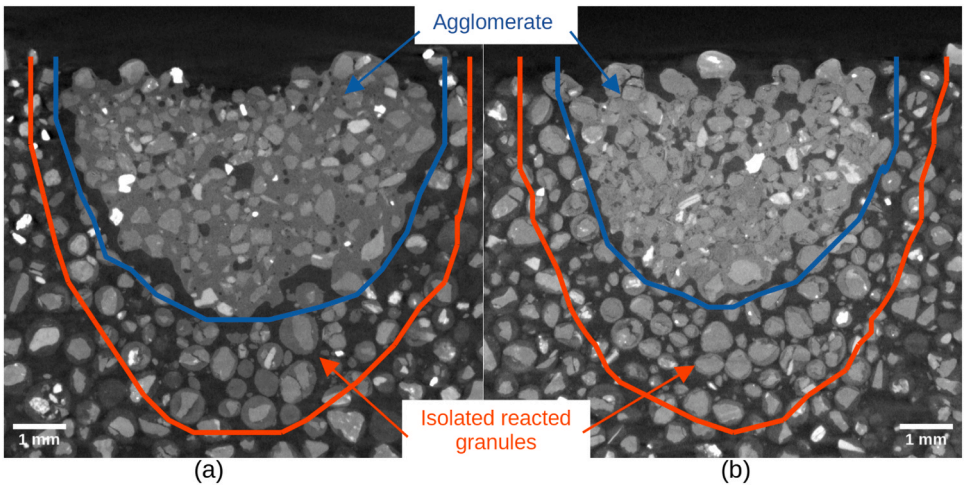

Fig. 10. Vertical reconstructed slice, perpendicular to the surface of the deposit (a) Na20 solution (b) K16 solution.

between the blue and the red lines in Fig. 10) that have reacted with the solution. In this region, the layer of metakaolin surrounding the sand has a slightly higher gray level than the one observed on the more distant granules, but the morphology remains unchanged. The reaction with these granules certainly took place at a later stage, shortly after the impact of the drop on the powder bed (typically in the monitoring time range between 0.033 and 10 s). The part of the solution that did not react on impact infiltrates more slowly, without detaching the metakaolin layer, allowing the granules to maintain their morphology. The area where these granules are present extends further below the agglomerate. Observations made on the two types of solutions were similar.

To provide a more precise description of the different observed zones, manual measurements were made from the images viewed along two perpendicular vertical axes. The results of these measurements corresponding to the two solutions are given in Table 4.

The values measured for both solutions are fairly close, although it can be noted that the K16 solution penetrates slightly further into the powder bed, as shown by the base/height ratios. The area where granules have reacted in an isolated manner also appears to be larger relative to the compact area for this solution. We can attribute the difference to the fact that K16 binder solution possesses a lower viscosity, compared to Na20 solution.

3.3. Development over time of the solution - granules mixture

The monitoring of the deposition of a drop of alkaline solution gave new insights into the first moments of interaction with the powder bed on a local scale. These tests were then complemented by monitoring the formation of the geopolymer matrix on a larger scale, as well as over longer periods of time, resulting from the reaction of MK30 granules with the Na20 and K16 solutions. A test was also performed with pure neutral water for comparison. Mixing was carried out in such a way as to closely respect the proportions of the alkaline solution and metakaolin powder generally used during the printing process. The voxel size was 5 µm and the size of the observed zone was 6x6x6mm^3. The first slice shows the initial metakaolin powder bed.

Table 4
Results of the two measurements carried out on the powder beds after interaction with a drop of Na20 solution and K16 solution. The following data are reported: average values for the base-diameter/height ratio of the agglomerated zone and the zone where isolated granules have reacted, Diameter ratio and Height ratio between the isolated reacted granules zone and the compact zone.

Solution	Base diameter / Hemisphere height		Isolated reacted granules region / Compact zone	
	Compact zone	Isolated reacted granules	Diameter ratio	Height ratio
Na20	0.68	0.88	1.07	1.38
K16	0.73	0.91	1.18	1.46

3.3.1. Reaction between MK30 and Na20

A first acquisition was performed in order to characterize the powder bed. Then the drops of solution were deposited in the straw.

Fig. 11 shows reconstructed slices extracted along the vertical axis at different steps of the monitoring, between 3 min and several hours after saturation. The reaction between the alkaline solution and the reactive metakaolin was very fast. Within just 3 min after the solution was deposited, a homogeneous mixture was visible around the sand particles, filling all voids initially present in the powder bed. Only small circular-shaped residual pores were visible (dark color). Some blurring can be seen in the first images due to the very fast evolution of the microstructure compared to the scan time.

A vertical displacement (upwards) of the powders between the initial state and the first state after solution deposition was observed. The observation area was adjusted to compensate for the packing of the powders. To keep the observation area approximately the same, a vertical movement of 1.8 mm was applied. The main changes then visible are the densification of the mixture (highlighted by the fact that the sand particles come closer together) and the movement of a few air bubbles over short distances. After around 7 h, some cracks appeared, due to constrained shrinkage caused by evaporation of water.

3.3.2. Reaction between MK30 and K16

The reaction of the granules with the K16 alkaline solution was monitored using the same method (supplementary material, Figure S9). The evolution of the K16 solution/metakaolin granules mixture is quite similar to the one observed for the Na20 solution. The reaction is very fast, with significant densification right from the start, as evidenced by the tracking of sand particles. This leads to a certain amount of blurring in the first instants of monitoring. Air bubbles are also present, and movement (relative to the sand particles) is more pronounced than in the case of the Na20 solution due to the lower viscosity of the K16 solution. The sand particles move downwards, while the voids remain at the same level, or even move upwards in some cases. As observed with the Na20 solution, cracks appear after a few hours.

3.3.3. Reaction between MK30 and water

The same procedure was used to follow the interaction of the MK30 powder with water, for a comparison with the alkaline solutions. The

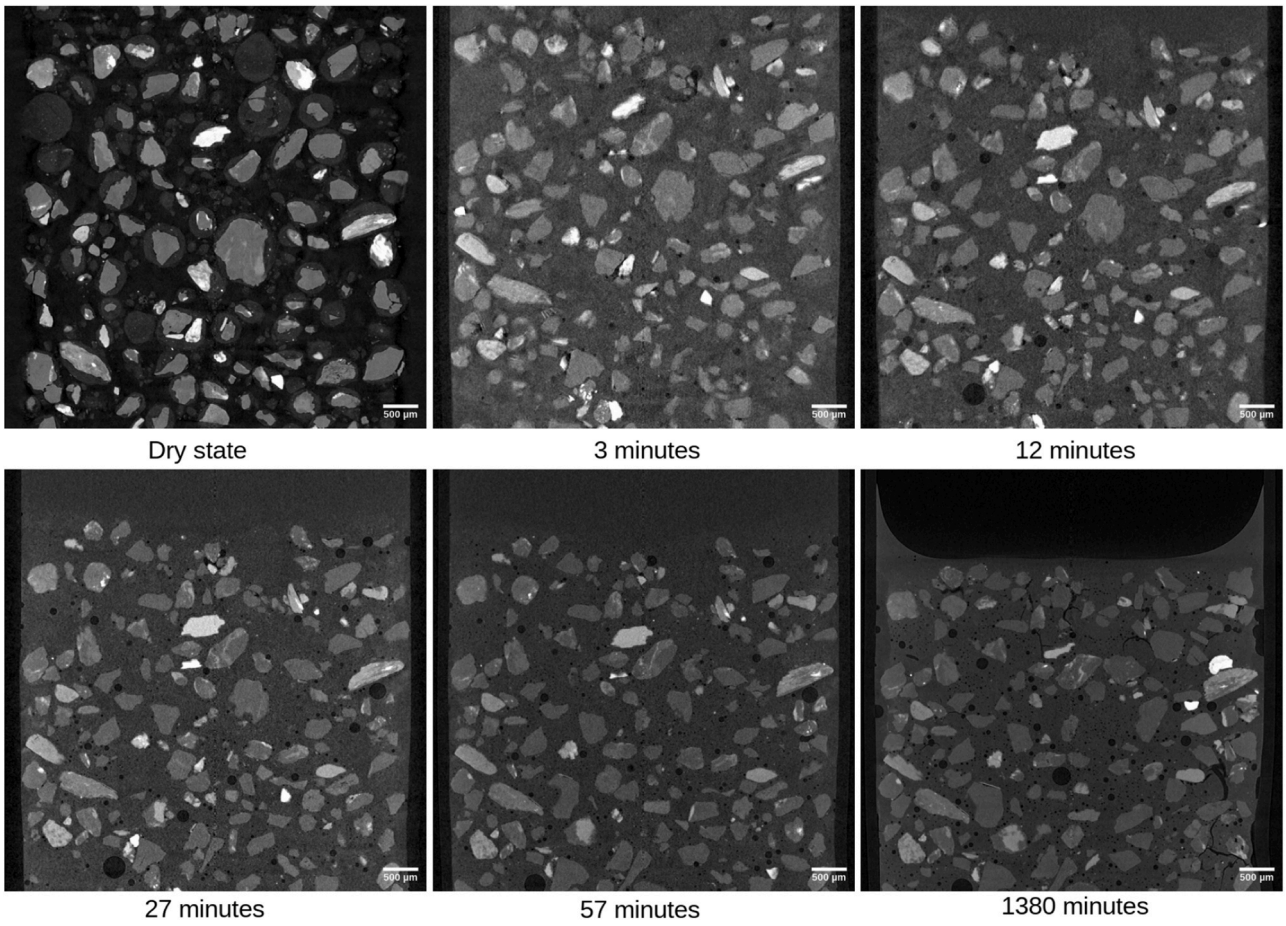

Fig. 11. Vertical reconstructed slices collected during monitoring of the reaction between Na20 alkaline solution and metakaolin granules. The initial state before liquid deposition is presented, followed by observations obtained via 3-minute scans with increasing spacing over time, up to around 24 h, see (supplementary material, Fig. S8).

reconstructed slices (supplementary material, Figure S10) show the evolution of the microstructure over time. The arrangement of sand particles is significantly less disturbed than with alkaline solutions. No significant densification was noticed during the first hour and a half, and the monitoring was carried out without adjusting the vertical position of the observation zone after the water was deposited. The scan taken after two hours shows a vertical contraction, and the scan acquired after around 17 h reveals a significant lateral contraction. These variations were probably linked to water evaporation. The numerous air bubbles observed coalesce at the end of monitoring, giving rise to large cavities. In the case of a reaction with water, cracks are not detected, but the material has no mechanical strength.

Fig. 12 shows a comparison of zoomed-in reconstructed slices of the initial states of MK granules (Figs. 12a and 12c) and just after Na20 solution or water deposition (Figs. 12b and 12d, respectively) These images confirm the very fast reaction of the alkaline solution with the metakaolin. The mixture between the sand particles is already very homogeneous after 3 min, when the alkaline solution reacts with MK forming a geopolymer gel that converts to a hard matrix bonding the sand particles. On the contrary, when water is used, the mixture is not so homogeneous and there is evidence of a much larger residual porosity. Water was also visible between these particles, with no reaction with metakaolin particles, as indicated by the heterogeneous grey levels observed among the sand particles (Fig. 12d). Very importantly, however, the images confirm that metakaolin particles detached from the sand due to the effect of the presence of the liquid, partially filling the voids between the granules. This is a very significant result, as it indicates that the concept of coating larger particles with fine particles, which by themselves couldn't be used to obtain a more compact flowable powder bed, is a viable strategy for obtaining a denser final part after binder jetting.

To highlight the densification of the mixture, the volume fraction of sand particles (likely to be inert during the reaction) was calculated using different monitoring steps, as shown in Fig. 13. Quantification was restricted to a size of 3.35 × 3.35 × 2.6 mm in the bulk of the material. A slight difference in the density of the starting powder bed was observed between the test with the Na20 solution (0.205) and the one with the K16 solution (0.235). During the reaction, densification followed the same trend, with a faster process during the first hour. After 24 h, the observed values were 0.34 for the Na20 solution and 0.35 for the K16 solution. The tomography images do not allow for a direct observation of the end of the reaction, but the changes visualized during monitoring enable us to estimate the time required to achieve it. Based on the movement of sand particles and air bubbles in the liquid system and the appearance of cracks in the solid, we can estimate that most of the consolidation reaction has taken place within a few hours.

Concerning the water, the behavior is clearly different, with the sand volume fraction remaining stable for almost 2 h. Then, densification occurs but is more limited than with the alkaline solutions (sand volume fraction of 0.317). The presence of a higher number of large pores can partly explain the difference. Furthermore, in the case of an alkaline solution, the geopolymer gel was created due to MK dissolution, which may flow faster than MK particles, resulting in a densification effect.

Characterizations were also conducted at higher resolutions to monitor the development of geopolymerization in more detail over time. Fig. 14 shows slices from high-resolution acquisitions from 1 day

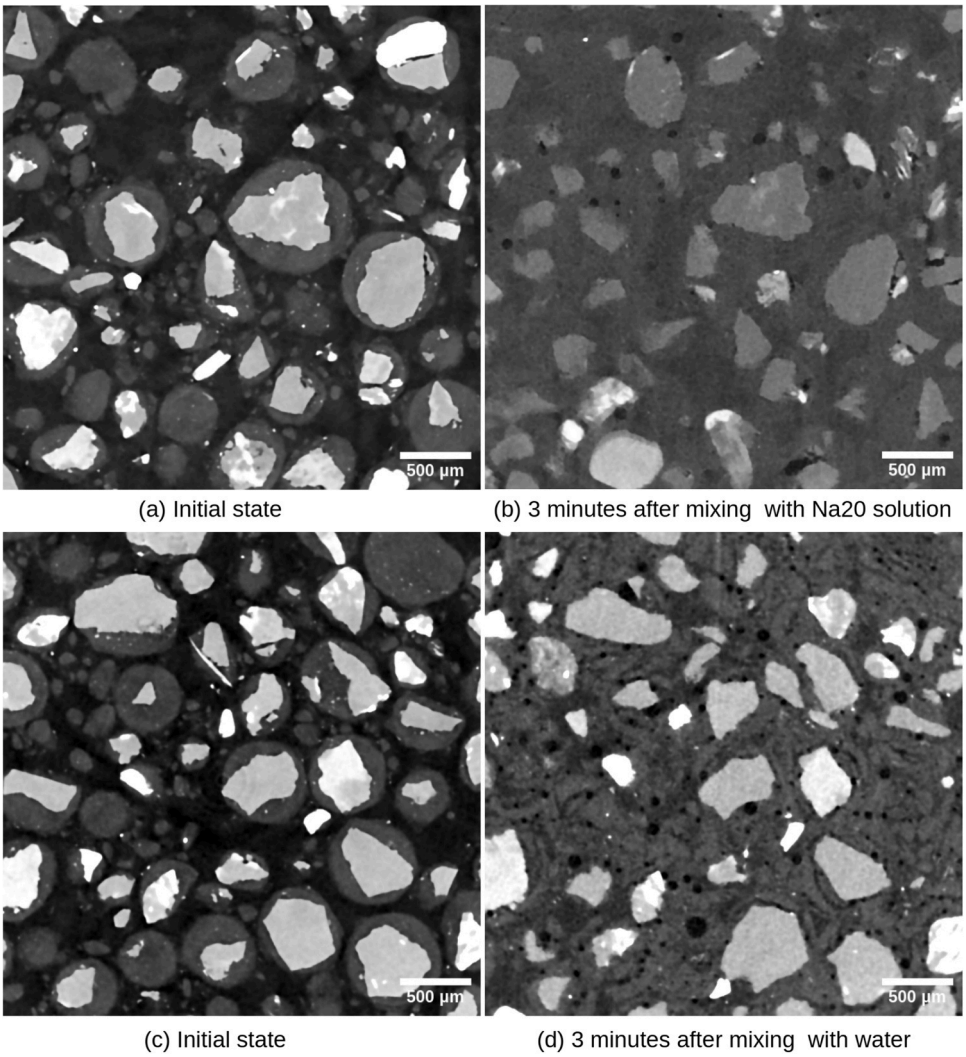

Fig. 12. Zoom on horizontal reconstructed slices a) Initial powder bed b) same powder bed at 3 min after saturation with Na20 alkaline solution c) Initial powder bed d) same powder bed at 3 min after saturation with water.

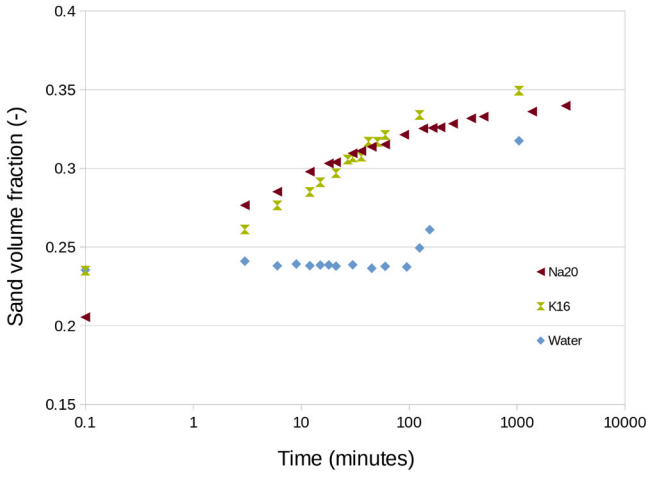

Fig. 13. Evolution of sand volume fraction over time for mixtures of metakaolin granules binder jetted with alkaline solution) Na20 or K16) or water.

after saturation between metakaolin granules (MK30) and Na20 solution. As observed on medium-resolution monitoring, cracks became visible in the geopolymer matrix after one day (as shown in the red ellipse). During the first 7 days, the development and growth of new cracks were observed. After 14 days, a different mechanism was revealed. Some existing cracks began to heal (as shown in the green ellipse). Gradually, more and more cracks were filled by a phase that is brighter than the polymer matrix (as illustrated by the orange arrow). Fine crystals were also observed on the walls of some pores (as indicated by the blue arrow).

At the same time, new cracks were appearing and developing, as can be seen after 35 days, indicating that even after such a long time the processes involved were not yet complete (precipitation of new phases, evaporation of water, etc.).

In their study, Trincal et al. [16] were interested in evaluating the autogenous deformation and desiccation shrinkage of a metakaolin-based geopolymer activated with sodium silicate solution. The authors described the shrinkage process in three phases. First, after drying for a few hours, the connected meso-pores of the geopolymer matrix started to empty. The movement of water created a depression, which caused mechanical stress at the origin of the shrinkage and probably of the cracks observed during our monitoring. In the second phase, the pores that act as reservoirs should empty over several weeks without generating significant additional stress. Finally, once the material is almost dry, the adsorbed water decreases and the capillary depression increases. Thus, higher stress is generated and the shrinkage of the material increases significantly.

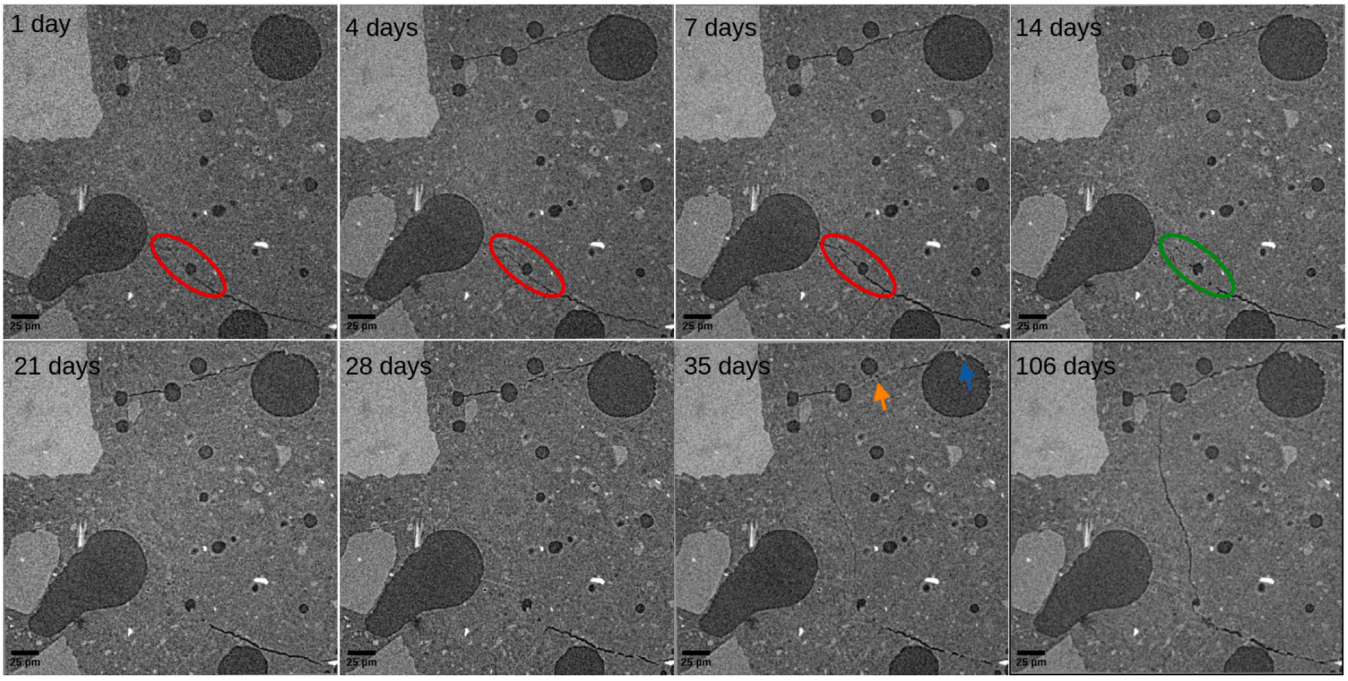

Fig. 14. High-resolution acquisition (voxel size 0.3 µm) was carried out at different times on a mixture of Na20 alkaline solution/metakaolin granules. The first acquisition shown was made 1 day after saturation, and the last after 106 days, see (supplementary material, Fig. S11).

The precipitation of salt crystals was also mentioned in [16,22], although it could not be observed by scanning electron microscopy. This phenomenon can be linked to the increased concentration of ions (mainly sodium) in the pore solution of the geopolymer. When super-saturation is reached, these ions precipitate in the form of minerals, salt, possibly hydroxides or carbonate. Thus, the brighter phase observed in our study could correspond to the precipitation of these types of crystals. Furthermore, in our tests, the stress impact may be increased by the confinement in the polymer tube during shrinkage, resulting in more cracks than a piece printed in the powder bed which can easily relax the stress due to the geopolymer formation shrinkage. It would be interesting to assess the positive effect that crack healing might have on the strength development in the material [36], even though detrimental effects concerning a decrease in the durability of the system can be expected.

3.4. Printed parts (with Na20 and K16 solutions) characterizations

The printed parts were characterized at different scales. Figs. 15 and 16 show reconstructed slices obtained from acquisitions with a voxel size of 5 µm (a) and 0.3 µm (b) for printed components by binder jetting of Na20 and K16 solutions respectively.

At the global scale (voxel size of 5 µm), macro-porosities are observed in materials made from both types of solution. Cracks are also present in the geopolymer matrix, generally with a curved shape. They do not appear to be uniformly distributed throughout the matrix but are rather grouped together in certain locations. They may have several branches. At least some of these cracks could be attributable to the cutting effect caused by diamond saw cutting to make geometric samples used for these analyses. At a more local scale (voxel size of 0.3 µm), meso-porosities with a size of a few microns or less are also observed, as well as fine cracks. The cohesion between the geopolymer matrix and

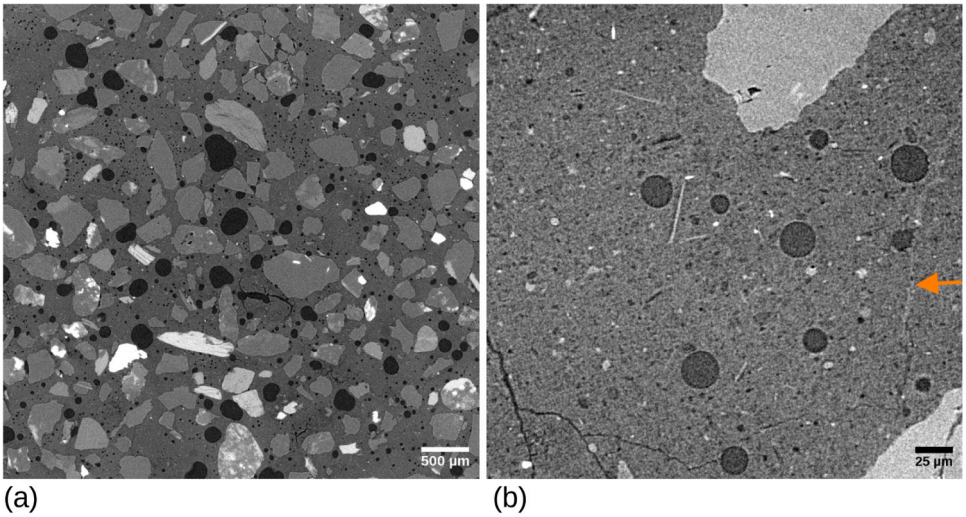

Fig. 15. Reconstructed slices of the MK30_Na20 printed part. (a) 5 µm voxel size (b) 0.3 µm voxel size.

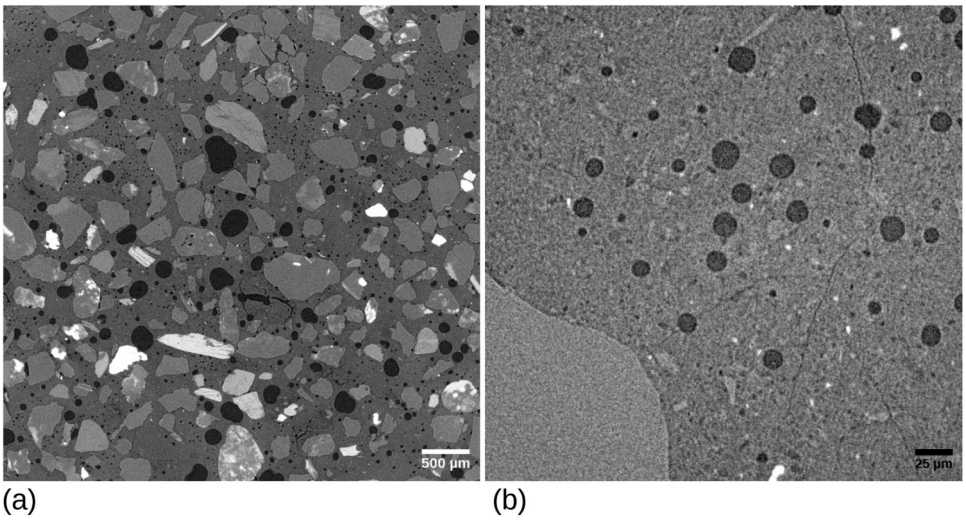

Fig. 16. Reconstructed slices of the MK30_K16 printed part. (a) 5 µm voxel size (b) 0.3 µm voxel size.

the sand particles appears to be high, which can be expected due to the chemical nature of both materials, and there are no cracks or porosities at the interface. The main differences between the two solutions are as follows:

- more cracks are visible in the material obtained using the Na20 solution. In particular, the Na20 solution is more viscous than the K16 one, and contains more water and this may lead to increased matrix stress and cracking during drying;
- some cracks in the matrix obtained with the Na20 solution, as observed during high-resolution monitoring, can be filled by the presence of a phase with high attenuation. A partially filled crack (vertical line lighter than the matrix) is highlighted by an orange arrow in Fig. 15b. This was not observed in samples produced using the solution K16, but it is important to note that at this resolution only a limited volume is analyzed:
- it seems that there is a greater amount of meso-porosity in the material printed with the Na20 solution. These porosities are more abundant than in the matrix observed during high-resolution monitoring, where very few were observed even after more than 100 days. This discrepancy could be attributed to how the alkaline solution was combined with the metakaolin granules. In fact, 3D printed samples remained under the powder bed for one day, then they were sealed in a bag for curing at room temperature. In the in-situ test, we assume that the system is open to air and water release, and porosity development may be variable and limited. Furthermore, the meso-porosity in samples produced using the sodium solution is often larger than that for samples obtained with the potassium solution (100 nm and beyond vs. a few nm);
- only a few unreacted granules were observed in the MK30_Na20 material and none in MK30_K16. The finding is understandable since the Na20 solution is more viscous than the K16 solution, resulting in less spreading/adsorption of the Na20 solution, leaving potentially few partially/unreacted granules in the printed part.

The quantification of porosities was achieved using images at 5 µm voxel size on a 5 x 5 x 5 mm volume. The volume fraction of macro-porosity (>10 µm) is 5.3 % for Na20 and 7.55 % for K16. Histograms of pore size are shown in Fig. 17. The dispersion is more pronounced in the case of Na20, with small porosities, and the presence of large porosities that can exceed an equivalent diameter of 1 mm.

The cracks observed by the acquisitions with a voxel size of 5 µm are highlighted in the 3D rendering in Fig. 18. Only a cubic sub-volume with sides of 1.5 mm is shown. This allows the morphology and distribution

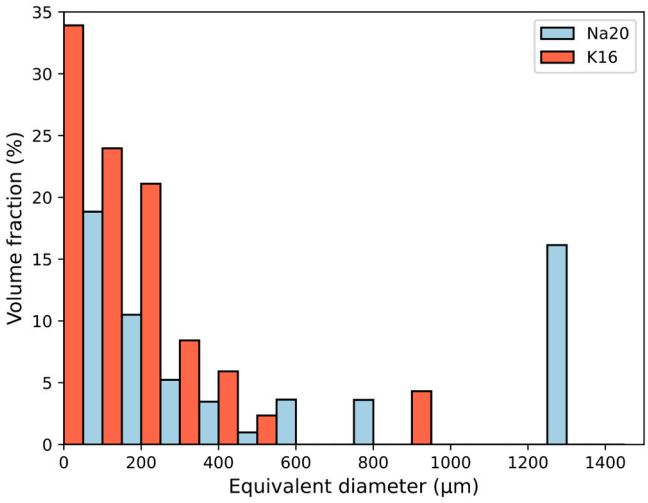

Fig. 17. Histogram representing the macro-porosity equivalent diameter (with an equivalent diameter larger than 10 µm) (a) MK30_Na20 (b) MK30_K16.

of the cracks to be better visualized. For the material made from the Na20 solution, some areas show numerous curved portions that are strongly connected to each other. The volume fraction of cracks is estimated at 0.85 % for sample MK30_Na20 and 0.45 % for sample MK30_K16.

Finally, quantification of the sand volume fraction was carried out based on 5 µm voxel size images. The volume fraction of sand calculated is 37 % for the material made with the Na20 solution and 38 % for the material made with the K16 solution. These values are in agreement with those observed during geopolymerization monitoring at the same resolution, with values approaching 35 % after about 24 h for both solutions.

Acquisitions were also made at a more extended scale (voxel size of 15 µm) to evaluate the influence of the process on the homogeneity of the printed parts. Analysis of the data obtained did not reveal the presence of areas with a higher amount of porosity in relation to the printing process, as it was previously observed [7]. The porosities are distributed relatively homogeneously in the geopolymer matrix, in any case without any direct correlation with the voxel size and/or layer thickness of the printer.

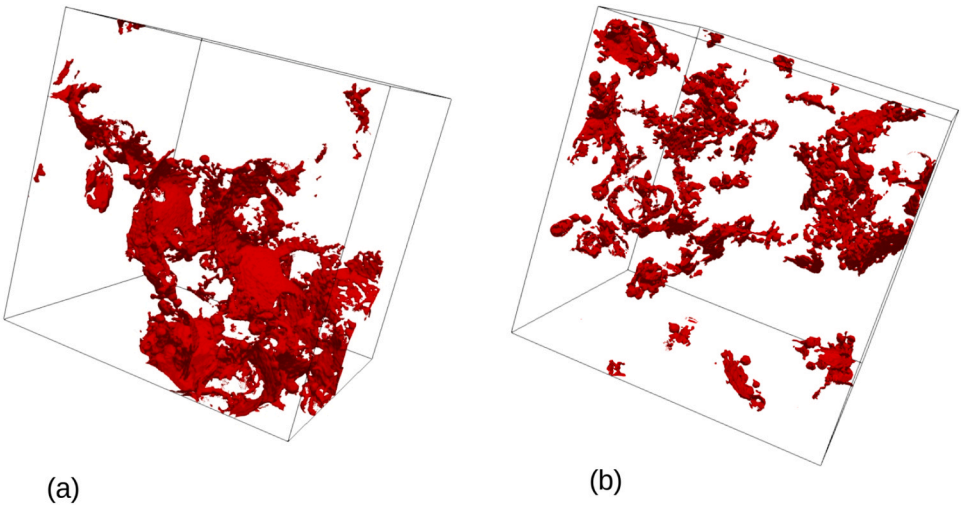

Fig. 18. 3D rendering of cracks: (a) MK30_Na20; (b) MK30_K16.

3.5. Results of other characterizations (NMR analysis and mechanical properties)

The mechanical tests were conducted 28 days after the binder jetting printing process and are expressed as the average between the perpendicular and parallel loading directions relative to the layer stacking. This approach is based on previous research [23], which demonstrated that the mechanical properties are independent of the loading direction for Na-based samples. Table 5 presents the data obtained in this study alongside the results from the aforementioned research [23]. The findings are consistent with prior observations: MK30_K16 samples containing 30 wt% MK achieved compressive and flexural strengths of ≈ 17 MPa and 7 MPa, respectively, while samples with MK30_Na20 yielded values of approximately ≈ 19 MPa and 8 MPa, respectively. Both materials possessed similar porosity levels of around 29 vol%, which is significantly lower than the value typical of parts produced using BJP [37].

As reported in the literature, the activation efficiency of sodium-based alkali activators is higher than that of potassium-based activators. Consequently, Na-based geopolymers generally exhibit higher mechanical strength, partly due to differences in matrix pore size and distribution compared to K-based systems [38,39]. This is consistent with our findings, where the Na20 samples demonstrated higher strength and lower variability than the K16 samples. The large cracks observed in the CT scans, especially in the K16 specimens, can be attributed to differences in curing behavior and sensitivity during sample preparation. While the two solutions resulted in distinct microstructural and mechanical characteristics, they behaved similarly in that both enabled successful geopolymerization following binder jetting.

As suggested by the xCT analysis of both the reacted powder bed and the printed parts, the activation solutions produced a similar microstructure and led to comparable strength values. The lack of large defects, which might have been generated by the impact of solution droplets with the powder bed, combined with the reactivity and densification reactions between the solution and metakaolin, leads to low porosity and high mechanical properties values. These results are superior to those achieved with magnesium phosphate cement binders [7] and other similar geopolymer-based binder jetted materials [34,40].

The NMR analysis confirmed the formation of the geopolymeric network, showing a high degree of reaction (>93 % for both the Na-based and K-based systems). The quantitative analysis is reported in Table 6. It is well known from the literature that metakaolin powder produces a characteristic aluminum NMR spectrum with three partially overlapped resonances centered at approximately 4, 29, and 58 ppm. These resonances are assigned to six-, five-, and four-coordinated aluminum, respectively, with a typical ratio of 27:35:38. The raised baseline in this spectrum is attributed to overlapping signals and related spinning sidebands, an effect of the incomplete averaging of second-order quadrupole couplings at the set spinning speed, as noted by Rocha et al. [41].

During the geopolymerization process, reaction with alkaline solutions leads to a significant reduction of the six- and five-coordinated aluminum, favoring the resonance at approximately 58 ppm. This resonance corresponds to tetrahedral aluminum in a 3D silico-aluminate network, which is typical of geopolymeric phases [33,42]. The aluminum-27 NMR spectra of the two reacted samples (Fig. 19) show the presence of only the four-coordination peak, indicating the formation of a tetrahedral network through the geopolymerization reaction of metakaolin. Tetrahedral network formation exceeds approximately 94 % in both the MK30_Na20 and MK30_K16 samples, with the MK30_K16 sample nearing complete tetrahedral network formation.

4. Conclusions

The sand-plus-metakaolin granulation process allowed to include a large (30 wt%) amount of fine metakolin particles in the feedstock, generating more spherical and regular-shaped particles with a limited increase in size, reducing at the same time the number of flat surfaces and edges hindering their free flow. Due to the good powder flowability, defect-free particle layers were deposited.

Table 5
Physical properties (density and porosity) and mechanical properties of parts printed with the Na20 and K16 solutions.

Sample name	Bulk Density (g/cm^3)	Total Porosity (vol %)	Compressive strength (MPa)	Bending strength (MPa)
MK30_Na20	1.71 ± 0.01	29 ± 1	18.5 ± 0.5	7.7 ± 0.2
MK30_K16	1.78 ± 0.01	29 + 1	16.6 ± 2.0	6.8 ± 0.2

Table 6
Quantitative analysis of the Al^{27} spectra with peak assignment.

%			
δ (ppm)	58.5	29.0	3.6
Assigned	Al(IV)	Al(V)	Al(VI)
MK	27.2	34.7	38.1
MK30_Na20	93.9	-	6.1
MK30_K16	98.5	-	1.5

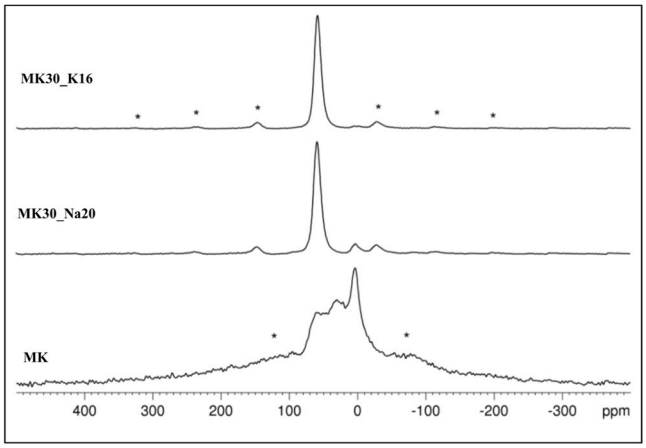

Fig. 19. ^{27}Al MAS NMR spectra of the three samples. Ssb (spinning side bands) are marked with *.

A compact powder bed, with no heterogeneity linked to the deposition of successive layers, was observed when the recoating system was used. The behavior of K-based and Na-based solutions was similar, although the lower viscosity of the potassium solution allowed better absorption into the powder bed and enhanced matrix homogeneity. X-ray computed tomography was used to monitor the real-time interaction between the alkaline solution and the powder bed, as well as the reaction kinetics leading to geopolymer formation, confirming that metakaolin activation was successfully achieved without mechanical mixing using binder jetting, leading to the manufacturing of large geopolymer parts with adequate strength, suitable for construction applications. NMR analysis confirmed the successful formation of a geopolymeric network in both sodium- and potassium-based systems, with the geopolymerization reaction proceeding to a very large extent.

Beyond the technical findings, this study makes a significant contribution to the field of sustainable additive manufacturing. By demonstrating effective large-scale binder jetting of geopolymers without the need for mechanical mixing of the two-component system before shaping, it provides a pathway for producing low-carbon, high-performance construction materials as alternatives to Portland cement or other binders. This approach also creates new opportunities for the automated, energy-efficient production of structural or refractory components. Furthermore, the insights gained into powder bed design, binder-powder interaction, and matrix formation deepen our understanding of binder jetting processes and support the broader adoption of environmentally friendly materials in scalable construction applications.

CRediT authorship contribution statement

Hamada Elsayed: Writing – review & editing, Writing – original draft, Visualization, Validation, Software, Project administration, Methodology, Investigation, Formal analysis, Data curation, Conceptualization. **Jérôme Adrien:** Writing – review & editing, Writing – original draft, Visualization, Validation, Software, Methodology, Investigation, Formal analysis, Data curation. **Filippo Gobbin:** Writing – review & editing, Visualization, Validation, Software, Methodology, Investigation, Formal analysis, Data curation. **Antonino Italiano:** Writing – review & editing, Software, Methodology, Data curation. **Éric Maire:** Writing – review & editing, Supervision, Resources, Supervision, Funding acquisition. **Paolo Colombo:** Writing – review & editing, Supervision, Resources, Funding acquisition, Conceptualization.

Declaration of Competing Interest

The authors declare the following financial interests/personal relationships which may be considered as potential competing interests: Paolo Colombo reports financial support was provided by European Commission. Eric Maire reports financial support was provided by European Commission. If there are other authors, they declare that they have no known competing financial interests or personal relationships that could have appeared to influence the work reported in this paper.

Hamada Elsayed: Writing – review & editing, Writing – original draft, Visualization, Validation, Software, Project administration, Methodology, Investigation, Formal analysis, Data curation, Conceptualization. Jérôme Adrien: Writing – review & editing, Writing – original draft, Visualization, Validation, Software, Methodology, Investigation, Formal analysis, Data curation. Filippo Gobbin: Writing – review & editing, Visualization, Validation, Software, Methodology, Investigation, Formal analysis, Data curation. Antonino Italiano: Writing – review & editing, Software, Methodology, Data curation. Éric Maire: Writing – review & editing, Supervision, Resources, Supervision, Funding acquisition. Paolo Colombo: Writing – review & editing, Supervision, Resources, Funding acquisition, Conceptualization.

Acknowledgements

This work was carried out in the framework of the projects: H2020-MSCA-RISE-2016 “AMITIE” (Additive Manufacturing Initiative for Transnational Innovation in Europe), contract no. 734342 and H2020-OTHER-EIT KIC RawMaterials Upscaling “IDEAL” (Industrial ResiDues for Smart FirE-resistAnt PhotocataLytic Components), proposal number 19040.

Appendix A. Supporting information

Supplementary data associated with this article can be found in the online version at doi:10.1016/j.addma.2025.104852.

Data Availability

Data will be made available on request.

References

[1] Y. Huang, M.C. Leu, J. Mazumder, A. Donmez, Additive manufacturing: current state, future potential, gaps and needs, and recommendations, J. Manuf. Sci. Eng. Trans. 137 (2015) 1–10, https://doi.org/10.1115/1.4028725.
[2] B.P. Conner, G.P. Manogharan, A.N. Martof, L.M. Rodomsky, C.M. Rodomsky, D. C. Jordan, J.W. Limperos, Making sense of 3-D printing: creating a map of additive manufacturing products and services, Addit. Manuf. 1 4 (2014) 64–76, https://doi.org/10.1016/j.addma.2014.08.005.
[3] Y. Lakhdar, C. Tuck, J. Binner, A. Terry, R. Goodridge, Additive manufacturing of advanced ceramic materials, Prog. Mater. Sci. 116 (2021) 100736, https://doi.org/10.1016/j.pmatsci.2020.100736.
[4] W.E. Frazier, Metal additive manufacturing: a review, J. Mater. Eng. Perform. 23 (2014) 1917–1928, https://doi.org/10.1007/s11665-014-0958-z.
[5] A.K. Pal, A.K. Mohanty, M. Misra, Additive manufacturing technology of polymeric materials for customized products: recent developments and future prospective, RSC Adv. 11 (2021) 36398–36438, https://doi.org/10.1039/d1ra04060j.
[6] G.J. Gibbons, R. Williams, P. Purnell, E. Farahi, 3D printing of cement composites, Adv. Appl. Ceram. 109 (2010) 287–290, https://doi.org/10.1179/174367509×12472364600878.
[7] F. Gobbin, H. Elsayed, A. Italiano, J. Adrien, P. Colombo, E. Maire, Large scale additive manufacturing of artificial stone components using binder jetting and their X-ray microtomography investigations, Open Ceram. 7 (2021) 100162, https://doi.org/10.1016/j.oceram.2021.100162.
[8] M. Amran, A. Al-Fakih, S.H. Chu, R. Fediuk, S. Haruna, A. Azevedo, N. Vatin, Long-term durability properties of geopolymer concrete: an in-depth review, Case Stud. Constr. Mater. 15 (2021) e00661, https://doi.org/10.1016/j.cscm.2021.e00661.
[9] L. Assi, E. Deaver, M.K. ElBatanouny, P. Ziehl, Investigation of early compressive strength of fly ash-based geopolymer concrete, Constr. Build. Mater. 112 (2016) 807–815, https://doi.org/10.1016/j.conbuildmat.2016.03.008.
[10] M. Vafaei, A. Allahverdi, Acid-resistant geopolymer based on fly ash-calcium aluminate cement, J. Mater. Civ. Eng. 30 (2018) 04018143, https://doi.org/10.1061/(ASCE)MT.1943-5533.0002321.
[11] M. Albitar, M.S. Mohamed Ali, P. Visintin, M. Drechsler, Durability evaluation of geopolymer and conventional concretes, Constr. Build. Mater. 136 (2017) 374–385, https://doi.org/10.1016/j.conbuildmat.2017.01.056.

[12] G. Franchin, H. Elsayed, R. Botti, K. Huang, J. Schmidt, G. Giometti, A. Zanini, A. De Marzi, M. D'Agostini, P. Scanferla, Y. Feng, P. Colombo, Additive manufacturing of ceramics from liquid feedstocks, Chin. J. Mech. Eng. 1 (2022) 100012, https://doi.org/10.1016/j.cjmeam.2022.100012.
[13] K. Komnitsas, D. Zaharaki, Geopolymerisation: a review and prospects for the minerals industry, Miner. Eng. 20 (2007) 1261–1277, https://doi.org/10.1016/j.mineng.2007.07.011.
[14] R. Si, Q. Dai, S. Guo, J. Wang, Mechanical property, nanopore structure and drying shrinkage of metakaolin-based geopolymer with waste glass powder, J. Clean. Prod. 242 (2020) 118502, https://doi.org/10.1016/j.jclepro.2019.118502.
[15] J. Davidovits, Geopolymers, J. Therm. Anal. 37 (1991) 1633–1656, https://doi.org/10.1007/bf01912193.
[16] V. Trincal, S. Multon, V. Benavent, H. Lahalle, B. Balsamo, A. Caron, R. Bucher, L. Diaz, M. Cyr, Shrinkage mitigation of metakaolin-based geopolymer activated by sodium silicate solution, Cem. Concr. Res. 162 (2022) 106993, https://doi.org/10.1016/j.cemconres.2022.106993.
[17] S. Chen, S. Ruan, Q. Zeng, Y. Liu, M. Zhang, Y. Tian, D. Yan, Pore structure of geopolymer materials and its correlations to engineering properties: a review, Constr. Build. Mater. 328 (2022) 127064, https://doi.org/10.1016/j.conbuildmat.2022.127064.
[18] G. Lazorenko, A. Kasprzhitskii, Geopolymer additive manufacturing: a review, Addit. Manuf. 55 (2022) 102782, https://doi.org/10.1016/j.addma.2022.102782.
[19] M. Xia, J. Sanjayan, Method of formulating geopolymer for 3D printing for construction applications, Mater. Des. 110 (2016) 382–390, https://doi.org/10.1016/j.matdes.2016.07.136.
[20] B. Panda, S.C. Paul, L.J. Hui, Y.W.D. Tay, M.J. Tan, Additive manufacturing of geopolymer for sustainable built environment, J. Clean. Prod. 167 (2017) 281–288, https://doi.org/10.1016/j.jclepro.2017.08.165.
[21] A. Averardi, C. Cola, S.E. Zeltmann, N. Gupta, Effect of particle size distribution on the packing of powder beds: a critical discussion relevant to additive manufacturing, Mater. Today Commun. 24 (2020) 100964, https://doi.org/10.1016/j.mtcomm.2020.100964.
[22] S.E. Brika, M. Letenneur, C.A. Dion, V. Brailovski, Influence of particle morphology and size distribution on the powder flowability and laser powder bed fusion manufacturability of Ti-6Al-4V alloy, Addit. Manuf. 31 (2020) 100929, https://doi.org/10.1016/j.addma.2019.100929.
[23] H. Elsayed, F. Gobbin, M. Picicco, A. Italiano, P. Colombo, Additive manufacturing of inorganic components using a geopolymer and binder jetting, Addit. Manuf. 56 (2022) 102909, https://doi.org/10.1016/j.addma.2022.102909.
[24] E. Maire, P.J. Withers, Quantitative X-ray tomography, Int. Mater. Rev. 59 (2014) 1–43, https://doi.org/10.1179/1743280413Y.0000000023.
[25] B. Aouan, S. Alehyen, M. Fadil, M. El Alouani, H. Saufi, M. Taibi, Characteristics, microstructures, and optimization of the geopolymer paste based on three aluminosilicate materials using a mixture design methodology, Constr. Build. Mater. 384 (2023) 131475, https://doi.org/10.1016/j.conbuildmat.2023.131475.
[26] A. Hawa, D. Tonnayopas, W. Prachasaree, Performance evaluation and microstructure characterization of metakaolin-based geopolymer containing oil palm ash, Sci. World J. 2013 (2013) 857586, https://doi.org/10.1155/2013/857586.
[27] V.F.F. Barbosa, K.J.D. Mackenzie, C. Thaumaturgo, Synthesis and characterisation of materials based on inorganic polymers of alumina and silica: sodium polysialate polymers, Int. J. Inorg. Mater. 2 (2000) 309–317, https://doi.org/10.1016/S1466-6049(00)00041-6.
[28] R. Fernandez, C. Moisy, Fijiyama, a registration tool for 3D multimodal time-lapse imaging, Bioinformatics 37 (2020) 1482–1484, https://doi.org/10.1093/bioinformatics/btaa846.
[29] J. Schindelin, I. Arganda-Carreras, et al., Fiji: an open-source platform for biological-image analysis, Nat. Methods 9 (2012) 676–682, https://doi.org/10.1038/nmeth.2019.
[30] M.D. Abramoff, P.J. Magalhaes, S.J. Ram, Image processing with ImageJ, J. Biophoton. Int 11 (2004) 36–42.
[31] J. Ahrens, B. Geveci, C. Law, ParaView: An End-User Tool for Large Data Visualization. Visualization Handbook, Elsevier, 2005, https://doi.org/10.1016/B978-012387582-2/50038-1.
[32] J.Y. Buffière, S. Savelli, P.H. Jouneau, E. Maire, R. Fougères, Experimental study of porosity and its relation to fatigue mechanisms of model Al-Si7-Mg0.3 cast Al alloys, Mater. Sci. Eng. A 316 (2001) 115–126, https://doi.org/10.1016/S0921-5093(01)01225-4.
[33] R. Dougherty, K. Kunzelmann, Computing local thickness of 3D structures with ImageJ, Microsc. Micro 13 (2007) 1678–1679, https://doi.org/10.1017/S1431927607074430.
[34] F. Zibouche, H. Kerdjoudj, J.-B.-E. Lacaillerie, H.V. Damme, Geopolymers from Algerian metakaolin. Influence of secondary minerals, Appl. Clay Sci. 43 (2009) 453–458, https://doi.org/10.1016/j.clay.2008.11.001.
[35] V. Voney, P. Odaglia, C. Brumaud, B. Dillenburger, G. Habert, From casting to 3D printing geopolymers: a proof of concept, Cem. Concr. Res. 143 (2021) 106374, https://doi.org/10.1016/j.cemconres.2021.106374.
[36] L.M. Seymour, J. Maragh, P. Sabatini, M. Di Tommaso, J.C. Weaver, A. Masic, Hot mixing: Mechanistic insights into the durability of ancient Roman concrete, Sci. Adv. 9 (2023) eadd1602, https://doi.org/10.1126/sciadv.add1602.
[37] N. Travitzky, A. Bonet, B. Dermeik, T. Fey, I. Filbert-Demut, L. Schlier, T. Schlordt, P. Greil, Additive manufacturing of ceramic-based materials, Adv. Eng. Mater. 16 (2014) 729–754, https://doi.org/10.1002/adem.201400097.
[38] Pe Cong, Y. Cheng, Advances in geopolymer materials: a comprehensive review, J. Traffic Transp. Eng. 8 (2021) 283–314, https://doi.org/10.1016/j.jtte.2021.03.004.
[39] A. Nmiri, O. Yazoghli-Marzouk, M. Duc, N. Hamdi, E. Srasra, Temperature effect on mechanical and physical proprieties of Na or K alkaline silicate activated metakaolin-based geopolymers, Ital. J. Eng. Geol. Environ. 1 (2016) 5–15, https://doi.org/10.4408/IJEGE.2016-01.O-01.
[40] A. Ur Rehman, V.M. Sglavo, 3D printing of geopolymer-based concrete for building applications, Rapid Prototyp. J. 26 (2020) 1783–1788, https://doi.org/10.1108/RPJ-09-2019-0244.
[41] J. Rocha, Single- and triple-quantum ^{27Al} MAS NMR study of the thermal transformation of kaolinite, J. Phys. Chem. B. 103 (1999) 9801–9804, https://doi.org/10.1021/jp991516b.
[42] F. Souayfan, E. Rozière, M. Paris, D. Deneele, A. Loukili, C. Justino, 29Si and 27Al MAS NMR spectroscopic studies of activated metakaolin-slag mixtures, Constr. Build. Mater. 322 (2022) 126415, https://doi.org/10.1016/j.conbuildmat.2022.126415.